Ore Geology Reviews 105 (2019) 572–589

Contents lists available at ScienceDirect

Ore Geology Reviews

journal homepage: www.elsevier.com/locate/oregeorev

Geology, geochronology, and geochemistry of the siruyidie'er prospect, Taxkorgan: A possible Miocene porphyry Mo ± Cu deposit in the Central Pamir

Ruihua Li[a,b], Hegen Ouyang[a,c,*], Jingwen Mao[a], Yongfeng Zhu[b]

[a] MNR Key Laboratory of Metallogeny and Mineral Assessment, Institute of Mineral Resources, Chinese Academy of Geological Sciences, Beijing 100037, China
[b] School of Earth and Space Sciences, Peking University, Beijing 100871, PR China
[c] State Key Laboratory of Ore Deposit Geochemistry, Institute of Geochemistry, Chinese Academy of Sciences, Guiyang 550081, PR China

ARTICLE INFO

Keywords:
Pamir
Porphyry deposit
Metallogenic potential
Tibetan
Continental crust

ABSTRACT

The Pamir and Tibetan plateaus, which have a similar terrane structure and evolutionary history since the Phanerozoic, are both host abundant Eocene to Miocene intrusions, however, unlike the Tibetan plateau, coeval porphyry deposits appear to be devoid in the Pamir plateau. In this study, we first report a potentially economic Cu-bearing sulfide mineralization at Siruyidie'er prospect in the Central Pamir. The Siruyidie'er prospect is characterized by the development of 14 breccia pipes in the north block and of Cu-bearing sulfide veins in the south block. Field evidence indicates that the brecciation and mineralization are intimately related to the intrusion of granite porphyry. Zircon U-Pb dating of the granite porphyry yields an age of 13.74 ± 0.21 Ma. This age overlaps with the hydrothermal muscovite $^{40}Ar/^{39}Ar$ data of 13.68 ± 0.17 Ma, which confirms the hydrothermal activity and mineralization at Siruyidie'er prospect are induced by the granite porphyry. The granite porphyries are shoshonitic in composition and have high K_2O (6.03–6.46 wt%; K_2O/Na_2O = 1.70–1.92), Ba (2983–3316 ppm), LREE (317–363 ppm) and Sr (331–378 ppm), and low MgO (0.54–0.63 wt%), Cr (6.73–8.28 ppm) and Y (7.88–9.91 ppm) contents. The rocks are LREE-enriched ($(La/Yb)_N$ = 53–66) and display weakly negative Eu (Eu/Eu^* = 0.79–0.87), positive LILES (Ba, Rb, and K) and negative HFSEs (Th, U, Nb, Ta, Ti, and Y) anomalies. They have enriched Hf isotopic compositions with $\varepsilon_{Hf}(t)$ values ranging from –8.78 to −5.01. The combined major and trace elements and Hf isotopic characteristics of the granite porphyries suggest that the primitive magmas were produced by high extent partial melting of an ancient crust source, possibly a thickened lower crust in the garnet stability field. A comparison of the granite porphyries at Siruyidie'er prospect with Eocene to Miocene ore-forming granitic porphyries of the Tibetan plateau reveals that the granite porphyries have lower water contents and originated from a continental crust rather than a depleted mantle source. Based on geological, compositional, and age data, we propose that the Siruyidie'er prospect has a potential to form porphyry Mo ± Cu deposit. This study provides the first direct evidence for the possible presence of porphyry Mo ± Cu deposit in the Pamir plateau.

1. Introduction

The Tibetan plateau is highly prospective for porphyry Cu ± Mo ± Au and associated epithermal Au ± Cu deposits of Eocene to Miocene age (Fig. 1), which are related to the post-collision extensional high-K calc-alkaline to shoshonite intrusions (Hou and Zhang, 2015; Richards, 2015). Examples include the Yulong (40.1 Ma) porphyry Cu-Mo deposit (Hou et al., 2006) in the Qiangtang terrane of eastern Tibetan plateau, the Machangqing (35.8 Ma) porphyry Cu-Mo deposit (Hou et al., 2007) in the Sanjiang orogen of southwest China, and the Qulong (16.4 Ma) porphyry Cu-Mo deposit (Yang et al., 2009) in the Lhasa terrane of south Tibet. The Pamir and Tibetan plateaus, both formed during the India-Asia collision since about 50 Ma (Mo et al., 2003; Van Hinsbergen et al., 2012), have a similar terrane structure and evolutionary history since the Phanerozoic (Yin and Harrison, 2000). Furthermore, Eocene to Miocene intrusions akin to those in the Tibetan plateau are also abundant in the Pamir plateau (Ke et al., 2006; Jiang et al., 2012; Chapman et al., 2018) (Fig. 1), especially

* Corresponding author at: MNR Key Laboratory of Metallogeny and Mineral Assessment, Institute of Mineral Resources, Chinese Academy of Geological Sciences, Beijing 100037, China.
E-mail address: ouyanghegen@cags.ac.cn (H. Ouyang).

https://doi.org/10.1016/j.oregeorev.2019.01.009
Received 21 September 2018; Received in revised form 31 December 2018; Accepted 10 January 2019
Available online 11 January 2019
0169-1368/

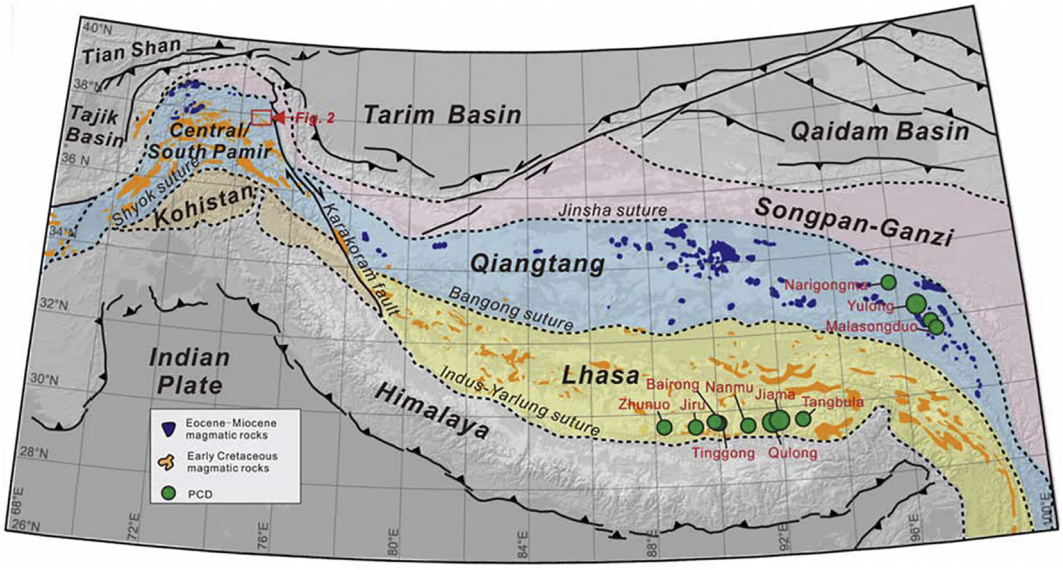

Fig. 1. Simplified geological map of the Pamir and Tibetan plateaus showing major blocks and temporal-spatial distribution of Cretaceous to Miocene magmatic rocks and Eocene to Miocene porphyry Cu deposits (PCD) (modified from Chapman et al., 2018).

in the Central Pamir, however, porphyry Cu ± Mo ± Au deposits appear to be devoid in this region but the reasons remain enigmatic.

Porphyry ore deposits are result from the shallow porphyritic intrusions of intermediate to felsic in composition that source most of the metals (Sillitoe, 2010). Thus, the geochemical signatures of the intrusions that might indicate the presence of porphyry ore deposits has direct implications for the evaluation of the metallogenic fertility of these intrusions, although magmatic fertility is not a sufficient condition for an igneous complex to produce a major porphyry ore deposit (Hedenquist and Lowenstern, 1994; Wilkinson, 2013). For example, the element ratio Sr/Y is effective in discriminating ore-forming intrusions from ordinary arc magmas in apparently unmineralized arc segments (Richards et al., 2012); initial Hf isotope composition of zircons may provide a screening method for identification of those that don't have the potential of forming porphyry Cu ± Mo ± Au deposit (Hou et al., 2015a); zircon Ce(IV)/Ce(III) ratios can be used to assess the economic potential of calc-alkaline intrusions for porphyry Cu ± Au mineralization (Ballard et al., 2002). Each of the above geochemical signals is merely permissive, that is, they all indicate a potential for, rather than the actual presence of, an ore body. Nevertheless, these signals allow suites of igneous rocks with low potential for ore formation to be ruled out so that exploration can focus on more prospective targets.

Recent exploration in the Taxkorgan, Central Pamir, led to the discovery of a potentially economic Cu-bearing sulfide mineralization associated with granitoids; this is referred to as the Siruyidie'er prospect (Fig. 2a). The mineralization consists predominantly of weakly veined and brecciated Cu-bearing sulfide in the Geierdikule and Siruyidie'er blocks (Fig. 2b), respectively. This pilot study focuses on the alteration and mineralization of the two blocks in the Siruyidie'er prospect, and petrology and geochemistry of ore-related intrusion, with a particular emphasis on evaluating the fertility potential for porphyry Cu ± Mo ± Au mineralization of Cenozoic magmatism in the Pamir plateau. To achieve these objectives, the major- and trace-element geochemistry, and zircon Hf isotopic compositions of the ore-forming intrusions in the Siruyidie'er prospect have been characterized and compared with their Tibetan Plateau equivalents. This approach has important implications for ore genesis, as well as economic significance in terms of exploration in the Central Pamir, and highlight, for the first time, the possible existence of porphyry Mo ± Cu deposit in the Pamir plateau.

2. Geological background

The Pamir plateau, which is part of a single contiguous orogenic plateau of the Pamir-Tibetan Plateau, is formed by accretion of a series of allochthonous Gondwanan continental fragments to the Asian continent during the Paleozoic to Mesozoic prior to the collision with India continent (Yin and Harrison, 2000; Robinson, 2015). It is composed of three broadly EW-trending continental terranes from north to south, i.e., the North Pamir, Central Pamir, and South Pamir-Karakoram terranes, and is surrounded by the Tarim basin in the east, the Tian Shan orogen in the north, and the Tajik basin in the west (Fig. 1).

The North Pamir lies between the Main Pamir Thrust to the north and the Late Triassic to Early Jurassic Tanymas suture (Burtman and Molnar, 1993) to the south. It was formed during a successively northward subduction and closure of Proto-Tethys and Paleo-Tethys oceans during the Paleozoic to Early Mesozoic (Yin and Harrison, 2000), and mainly consists of Paleozoic to early Mesozoic arcs and the Karakul-Mazar arc-accretion complexes like the Kunlun and Hoh Xil-Songpan-Ganzi terranes of northern Tibetan plateau (Robinson et al., 2012). The Central Pamir terrane is bounded by the Tanymas suture to the north and the Jurassic Rushan-Pshart suture (Schwab et al., 2004) to the south. It accreted to the North Pamir terrane along the Tanymas suture in the Late Triassic to Early Jurassic during the evolution of Paleo-Tethys ocean (Burtman and Molnar, 1993). The Central Pamir comprise Paleozoic–Jurassic platform rocks, gneiss domes, and Eocene to Miocene ultrapotassic to potassic igneous rocks (e.g., Vanj, Dunkeldik, and Taxkorgan complexes) laterally equivalent to the northern Qiangtang terrane (Kapp et al., 2000; Robinson et al., 2012). The South Pamir-Karakoram terrane, bound by the Rushan-Pshart suture to the north and the Late Jurassic to Early Cretaceous Shyok suture to the south, is generally interpreted to be continuous (Kapp et al., 2005; Robinson, 2009). It consists of Proterozoic gneiss, Paleozoic–Mesozoic metasedimentary rock, and Cretaceous granitoids equivalent to the southern Qiangtang terrane in Tibetan plateau (Robinson, 2009; Robinson et al., 2012).

Contemporary and after the aggregation of these terranes, different major strike-slip faults formed and offset the Pamir north relative to the Tibetan plateau (Yin and Harrison, 2000; Robinson et al., 2004). Although the Pamir plateau has a similar history of terrane accretion with

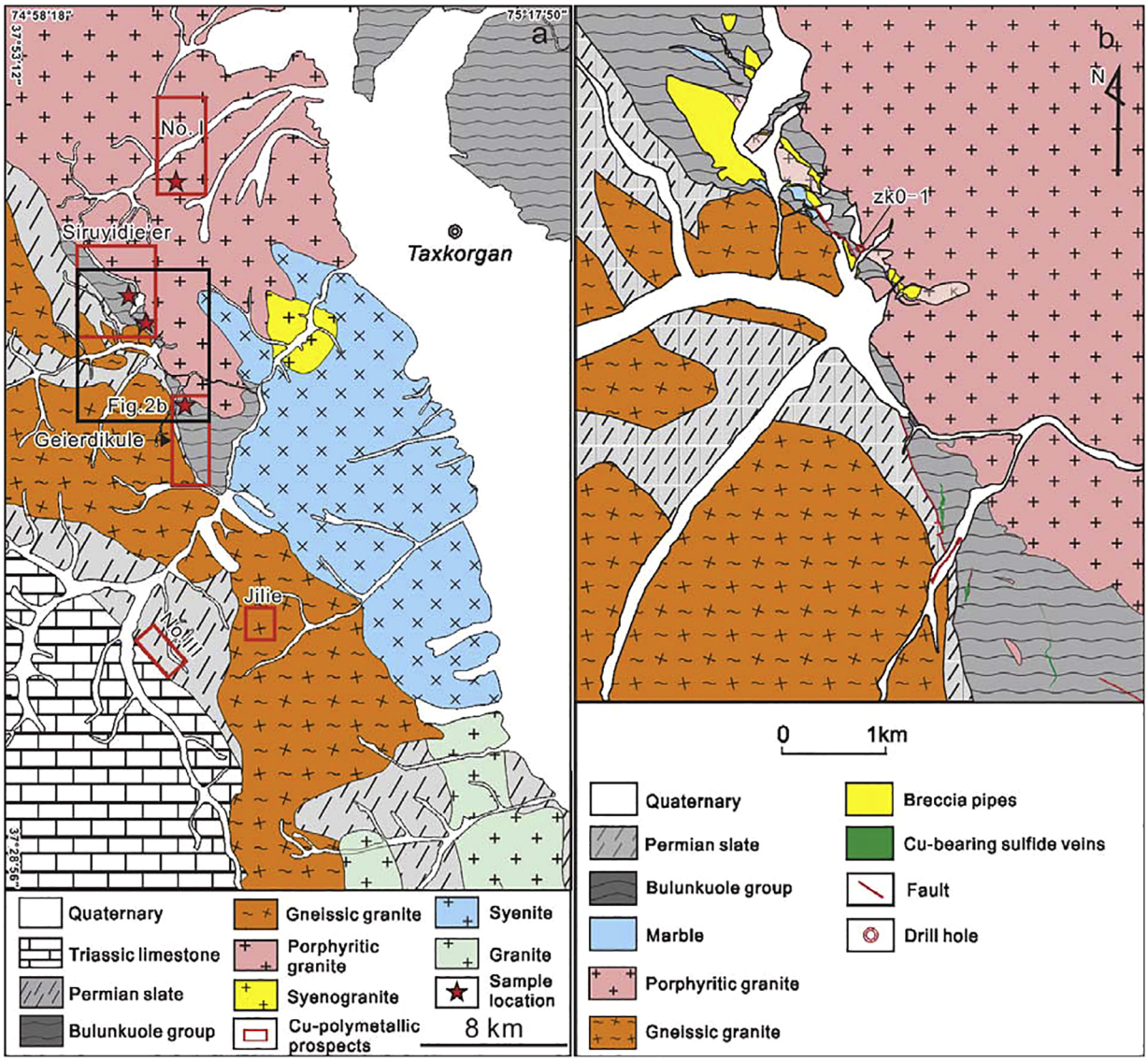

Fig. 2. (a) Regional geological map of the Siruyidie'er prospect showing the distribution pattern of Cu-polymetallic occurrences; (b) Geological map of the Siruyidie'er prospect showing the mineralization pattern at Siruyidie'er prospect (after from Ouyang et al., 2017).

the Tibetan plateau, it has experienced more intense deformation and shortening than the Tibetan plateau during the India-Asia collision since about 50 Ma (Mo et al., 2007; Van Hinsbergen et al., 2012), which have been bent into an arcuate shape and translated northward over the Tajik and Tarim basins (Fig. 1).

The most prominent structural feature in the Pamir plateau is the extensional system which extends EW for ca. 500 km and which manifested by the conspicuous gneiss domes (Schmidt et al., 2011; Stearns et al., 2015). Each of the three terranes of the Pamir plateau contains elongate medium- to high-grade crystalline domes, e.g., the Kongur Shan and Muztagh Ata domes in the North Pamir terrane, the Yazgulem, Sarez, Muskol, and Shatout domes in the Central Pamir terrane, and the Shakdhara and Alichur domes in the South Pamir-Karakoram terrane, that collectively make up ~20% of the rock exposed in the Pamir plateau (Schmidt et al., 2011). The domes are built of siliciclastic and carbonate metamorphic sedimentary rocks (e.g., high-grade schists and gneisses) which have been exhumed from a crustal depth of 30–40 km since Oligocene to Miocene times (Robinson et al., 2004; Robinson et al., 2007; Schmidt et al., 2011; Cao et al., 2013; Stearns et al., 2015), and intruded by volumes of ultrapotassic to potassic igneous rocks and leucogranits as young as Late Miocene (Schwab et al., 2004; Schmidt et al., 2011; Jiang et al., 2012).

Seismic data indicate that the Pamir mantle exhibits vigorous intermediate depth (> 100 km) seismicity (Sippl et al., 2013; Kufner et al., 2016; Li et al., 2018) and strong velocity anomalies even down to the bottom of the transition zone (Negredo et al., 2007; Li et al., 2018), which is rare in the Tibetan plateau. Intermediate-depth seismicity usually occurs in Benioff zone of the oceanic subduction zone (Stern, 2002), however, in the Pamir plateau it should be related to the subduction of Asian continent induced by the excessive amount of lithospheric shortening and thickening (Negredo et al., 2007; Robinson et al., 2012; Sippl et al., 2013; Kufner et al., 2016).

3. Regional geology

The research area (Fig. 2a) in this study is situated in Taxkorgan County, Central Pamir, near the Tajik-China border. This area is one of the least understood zones in Chinese Pamir because of extreme inaccessibility, and there is no consensus yet regarding its origin and evolution. Former studies suggest that this area is a part of South Kunlun orogen (i.e., North Pamir). However, our recent studies (Ouyang et al., 2017) indicate that the studied area can be tectonically

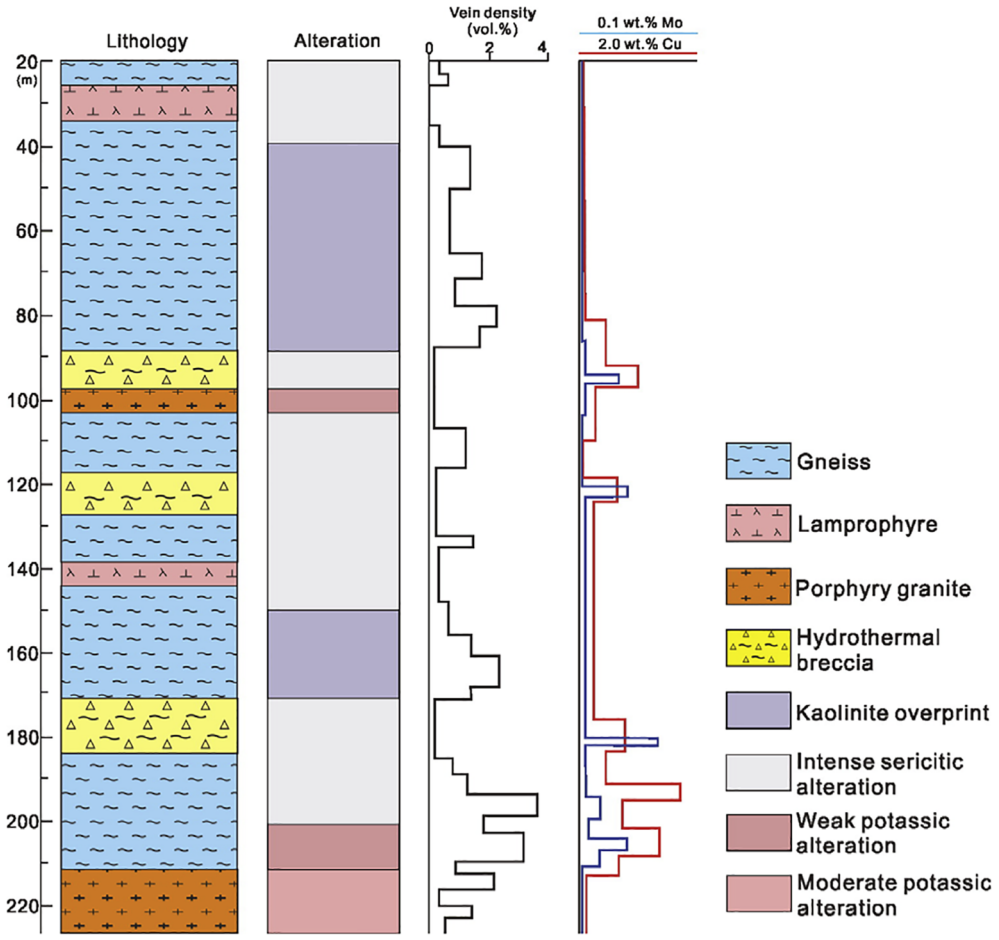

Fig. 3. Drill hole log showing lithology, alteration, vein density and Mo and Cu grades revealed from diamond drill hole zk0-1.

subdivided into two parts (i.e., the eastern and western parts) by the Taxkorgan fault. These two parts have significantly different sedimentary, metamorphic, and magmatic histories, and appear to have distinctive crustal compositions and terrane affinity.

The exposed oldest stratigraphic unit in the eastern part, known as "Bulunkuole Group", consists mainly of garnet gneiss, amphibole gneiss, schist, magnetite-bearing quartzite, and marble (Ji et al., 2011). The sedimentation age of the "Bulunkuole Group" although is still controversial, its metamorphic age is consensually assigned to the Late Triassic (Yang et al., 2010; Zhang et al., 2018). The "Bulunkuole Group" is locally overlain from bottom to up by Silurian metamorphic siltstone and volcanic rocks, Carboniferous metamorphic sandstone and siltstone, and Permian clastic stone, limestone, and volcanic rocks. Magmatic rocks within this part are dominantly by Triassic granitic rocks with subordinately Cambrian alkaline to granitic rocks, and Carboniferous and Cretaceous granitoids (Zhang et al., 2016; Zhang et al., 2018). Mineralization in this part is characterized by widespread occurrences of Precambrian Banded Iron Formation (Zhang et al., 2016; Zhou et al., 2017), e.g., the Zankan, Laobing, and Kalaizi iron deposits.

The basement of the western part comprises mainly of amphibole gneiss and biotite gneiss. Traditionally, this unit was named as "Bulunkuole Group", but no precise age data were available. Our recent study shows that the sedimentation age of this unit is ca. 2200–1800 Ma and its metamorphic age is ca. 790 Ma (Ouyang et al., 2017), contrasts sharply with those in the eastern part. The other units that overlain the basement are the Permian siliceous slate and marble, and Triassic dolomitic limestone (Fig. 2a). Four pulses of magmatism (Ouyang et al., 2017), i.e., Early Cambrian, Late Triassic, Early Cretaceous, and Miocene, have been identified in this unit. Early Cambrian and Early Cretaceous magmatism are rarely developed in the western part, the former comprises dikes of gabbro and two-mica granite, with zircon U-Pb ages of 525–520 Ma; the late consists of two-mica granite, with zircon U-Pb age of ca. 118 Ma. Another important stage of magmatism took place in the western part is in the Late Triassic. Isotopic dating of the gneissic granite defines an age of ca. 200 Ma. However, the most important stage of magmatism in this unit is the Miocene, known as the Taxkorgan complex which can be considered as part of a larger unit called the Dunkeldik-Taxkorgan complex (Chapman et al., 2018). The Taxkorgan complex is a regional unit composed by a set of high-K calc-alkaline and alkaline intrusions of intermediate to felsic composition. It consists of porphyritic granite, granite porphyry, syenite and syenogranite, and the latter two intrusions have emplacement ages of 12–10 Ma (Jiang et al., 2012). Hydrothermal alteration and low grade Cu-bearing mineralization occur throughout the research area, including the No. I Cu-Fe, Siruyidie'er Cu-Mo, Jilie Cu-Fe and No. III Cu prospects (Fig. 2a), but no resource estimates were published for the prospects with the exception of the Jilie prospect which has a reserve of 456 t Cu (Yang, 2007). At No. I prospect, Cu-Fe sulfides occur as veinlets in the fissures of porphyritic granite or as veinlets and disseminations in the skarn hosted by the Permian marble. Copper-Fe mineralization in the Jilie prospect occurs as veins and hydrothermal breccias hosted by the gneissic granite. The ore mineralogy consists of mainly chalcopyrite, pyrite and siderite. Mineralization at No. III Cu prospect occurs as quartz-veins and appears to be controlled by fracturing in a sequence of Permian slate (Ouyang et al., 2017).

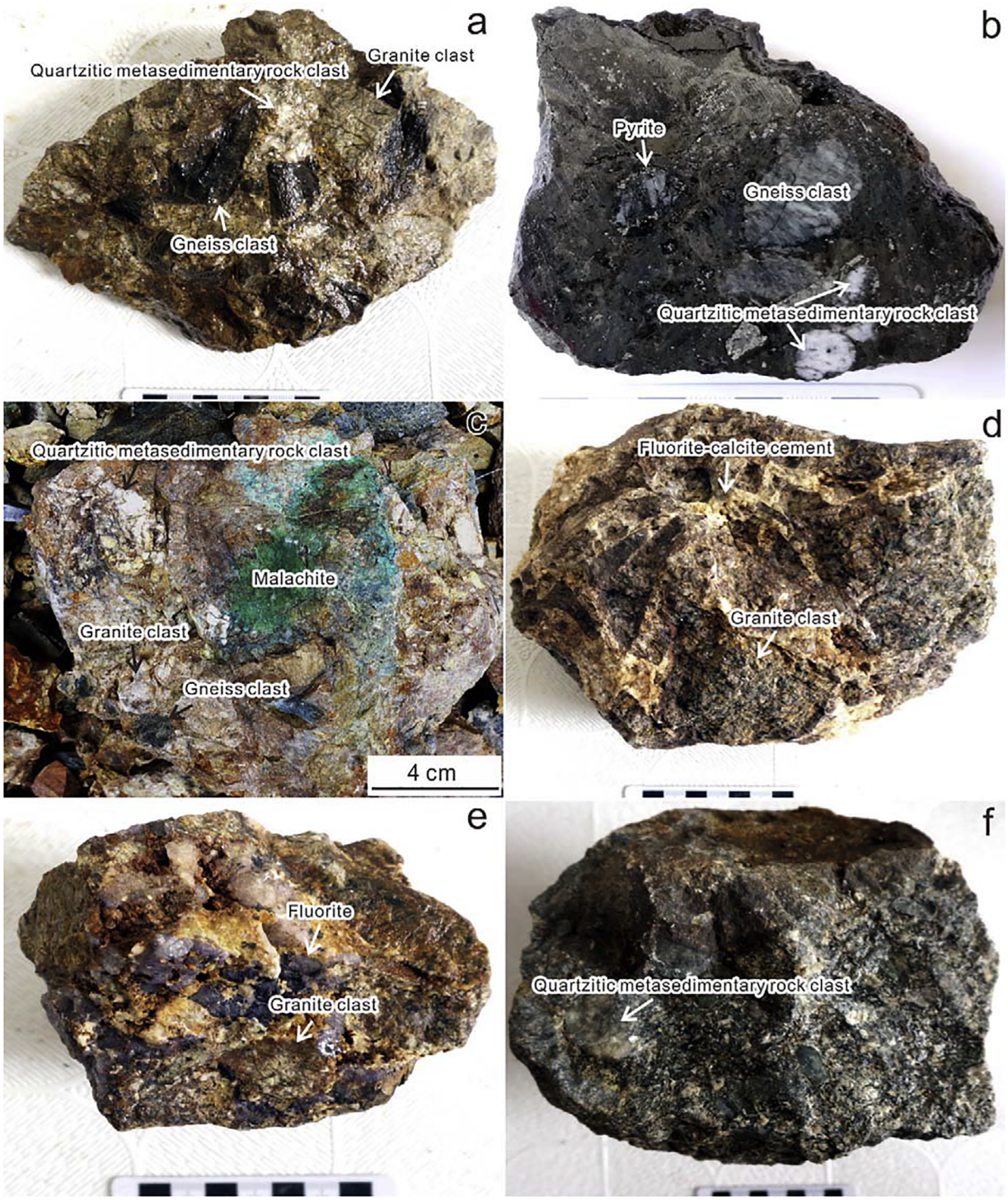

Fig. 4. Representative photographs of breccias from the Siruyidie'er block. (a) Magmatic breccia with felsic cement and gneiss, quartzitic metasedimentary rock and granite clasts; (b) Pyrite-rich hydrothermal breccia with chloritization of clasts of gneiss and quartzitic metasedimentary rock; (c) Copper-rich hydrothermal breccia; (d-e) Fluorite-rich breccia with fluorite and calcite cement and granite clasts; (f) Magmatic breccia with chloritization of felsic cement and quartzitic metasedimentary rock clast.

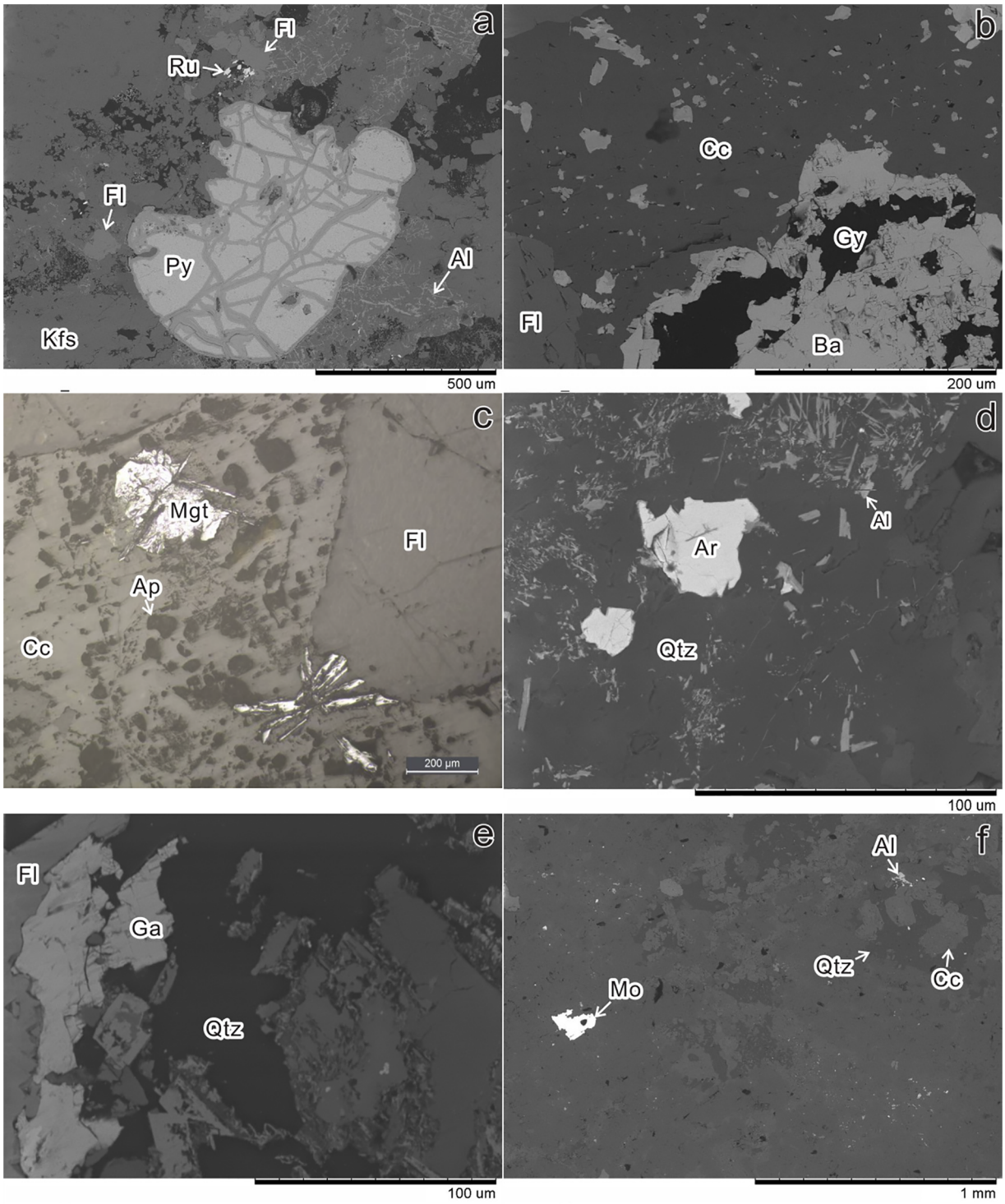

Fig. 5. Backscattered electron images showing the composition and texture of hydrothermal breccia's matrix from the Siruyidie'er block. (a) Fluorite, pyrite, allanite and rutile cements in the fluorite-rich hydrothermal breccia; (b) Fluorite, calcite, barite and gypsum cements in the fluorite-rich hydrothermal breccia; (c) Fluorite, calcite, magnetite and apatite cements in the fluorite-rich hydrothermal breccia; (d) Quartz, argentite and allanite cements in the pyrite-rich hydrothermal breccia; (e) Fluorite, quartz and galena cements in the fluorite-rich hydrothermal breccia; (f) Quartz, molybdenite, calcite and allanite cements in the pyrite-rich hydrothermal breccia. Mineral abbreviation: Al = allanite, Ap = apatite, Ar = argentite, Ba = barite, Cc = calcite, Fl = fluorite, Ga = galena; Gy = gypsum, Kfs = K-feldspar, Mgt = magnetite, Mo = molybdenite, Py = pyrite, Qtz = quartz, Ru = rutile.

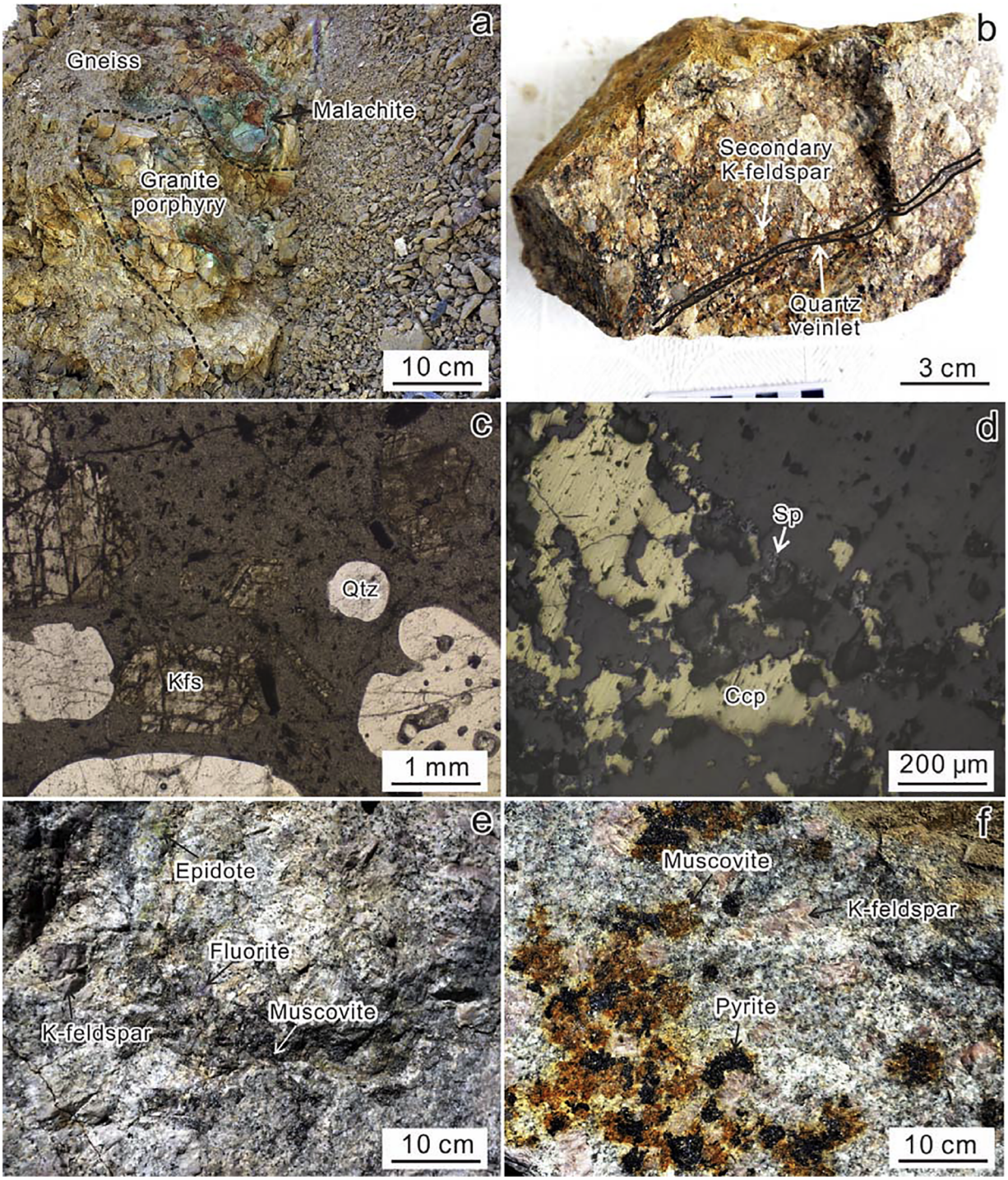

Fig. 6. Representative photographs and photomicrographs of mineralization and alteration from the Geierdikule block. (a) Outcrop showing Cu mineralization developed in and around granite porphyry; (b) High temperature potassic alteration and quartz veinlets developed in granite porphyry; (c) Photomicrograph showing phenocrysts in granite porphyry consist of K-feldspar and quartz; (d) Cu-bearing veinlet in granite porphyry consists of chalcopyrite and sphalerite; (e-f) Field photographs of porphyritic granite showing muscovite intergrown with pyrite, fluorite, and epidote within fissures. Mineral abbreviation: Ccp = chalcopyrite, Kfs = K-feldspar, Qtz = quartz, Sp = sphalerite.

4. Mineralization and alteration in the Siruyidie'er prospect

The Siruyidie'er prospect is the largest Cu-bearing mineralized prospect in the Taxkorgan area. It consists of the Siruyidie'er block in the north and the Gei'erdikule block in the south (Fig. 2b). Both blocks host low grade Cu and/or Mo mineralization but with contrast mineralization style.

The Siruyidie'er block composes of 14 breccia pipes which are vertically oriented, downward-tapering, polymict lithic rock unit that host to all of the significant alteration and mineralization. A proximal propylitic alteration, characterized by chlorite, epidote, and pyrite, is developed in and near the periphery of the breccia pipes. Deep drill holes (zk0-1; Fig. 2b, Fig. 3) in the Siruyidie'er block have revealed that low grade Cu and Mo mineralization, potassic alteration and brecciation are temporally and spatially associated with intrusion of the granite porphyry and igneous-hydrothermal breccias. Two types of breccia, magmatic and hydrothermal, are identified by clast lithology, clast shape, alteration degree, and composition of breccia matrix or cement. The magmatic breccia (Fig. 4a, f) is matrix-supported with a medium- to fine-grained matrix. The clasts are poorly sorted subangular to subrounded and consist of gneiss (~50%), quartzitic metasedimentary rock (~25%) and granite (~25%). The matrix consists of porphyritic felsic materials. Mineralization is rare in this type of breccia but when present they include pyrite and chalcopyrite. Hydrothermal breccia is the volumetrically most prominent breccia type at Siruyidie'er block. The hydrothermal breccia is a coarse, polymict clast-supported breccia with a cement composed of hydrothermal crystalline materials (Fig. 5b–e) and can be further divided into three types based on the components of cement, i.e., pyrite-rich breccia (Fig. 4b), Cu-rich breccia (Fig. 4c) and fluorite-rich breccia (Fig. 4d-4e). Cement in the fluorite-rich breccia, which envelopes angular to rounded aggregates of granitic clast (Fig. 4d–e), is mainly consisted of fluorite with minor pyrite, calcite, gypsum, barite, allanite, rutile, apatite, magnetite and galena (Fig. 5a–c, e). Pyrite-rich breccia is characterized by quartz-pyrite-calcite-allanite-molybdenite-argentite assemblage (Fig. 5d, f) cements and alters the gneiss and siliceous rock clasts (Fig. 4b). Rarely Cu-rich breccia can be found in the Siruyidie'er block. The clasts are poorly sorted subangular to subrounded and consist of gneiss (~25%), siliceous rocks (~25%) and granite (~50%) (Fig. 4c). The cement consists of malachite, pyrite and quartz.

Geierdikule block hosts the highest-grade Cu mineralization in the Siruyidie'er prospect. The exposed alterations in this block include moderate potassic alteration in granite porphyry (Fig. 6b) and weakly potassic alteration and widespread sericitic alteration in gneiss. Mineralization in this block occurs within granite porphyry and in the contact zone between granite porphyry and gneiss (Fig. 6a). Phenocrysts in the porphyry consist of K-feldspar (65–70%) and quartz (30–35%), which together account for 50–55% of the volume of the rock (Fig. 5b–c). The same minerals, accompanied by anhedral quartz and K-feldspar, are present in the groundmass (Fig. 5c). Accessory minerals in the granite porphyry include apatite, zircon, magnetite and ilmenite. K-feldspar is anhedral with tartan twinning. Quartz is euhedral to anhedral with a diameter of 0.5–3 mm. Veinlets of quartz ± chalcopyrite are present in the granite porphyry (Fig. 5b). The highest-grade zones of mineralization at Geierdikule block occur within the contact zone between granite porphyry and genesis (Fig. 5a). Mineralization appears to be controlled by tightly spaced subvertical fracturing. Highly fractured gneiss proximal to the granite porphyry hosts higher grades. The ore mineralogy at Geierdikule consists of veins with chalcopyrite-pyrite-sphalerite ± galena ± molybdenite (Fig. 5d). The alteration consists of high-temperature K-feldspar and medium- to low-temperature sericite ± chlorite-smecitite ± kaolinite.

5. Sample and analytic methods

Samples from the granite porphyry dike and magmatic breccia were collected from both outcrops and drill core. The sampling locations are indicated in Fig. 2a. Only the least altered samples were selected for zircon U–Pb dating and Hf isotope analysis, and whole rock major and trace elements analysis on the basis of hand lens and thin section observations. A hydrothermal muscovite sample was also extracted from a sulfide- fluorite-epidote vein sample from the No. I prospect (Fig. 6e–f) for incremental heating $^{40}Ar/^{39}Ar$ dating. The muscovite is coarsely crystalline and occurs together with pyrite, fluorite and epidote, representing the hydrothermal activity of Mo- and Cu-bearing mineralization.

5.1. Major and trace elements analysis

Fresh rock samples collected for major and trace element analyses were crushed in a steel crusher and then powdered in an agate mill to a grain size less than 200 mesh. The powder samples were then fluxed with $Li_2B_4O_7$ (1:8) to make homogeneous glass disks at 1250 °C using a V8C automatic fusion machine. The bulk rock major elements were analyzed on fused glass discs with a Zetium (PANalytical) sequential X-ray fluorescence spectrometer. The loss on ignition (LOI) of sample powders was determined at a temperature of 1000 °C. The measurements were monitored using the standards GSR-2 and GSR-22, and the accuracy of the analytical results was controlled by measuring the standard reference material BHVO-2. The analytical errors for the major element analyses were better than 2%.

Trace elements, including rare earth elements (REE), were measured using an Agilent 7500a ICP-MS system. During the digestion procedure, 25 mg of sample powder was precisely weighed and transferred into screw-top Teflon beakers. Then 1.5 ml HF and 1.5 ml HNO_3 were added in turn and heated in the closed Teflon beakers at 100 °C for 96 h, and subsequently opened and heated at 120 °C to evaporate the dissolution. Following this, 0.5 ml HF and 2.5 ml 1:1 HNO_3 were added, and the beakers were transferred into a digestion bomb. The bombs were heated in an oven at 170 °C for 72 h. Then the beakers were opened and heated at 120 °C to evaporate the dissolutions. The residues were added to 1:1 HNO_3, then sealed and heated at 120 °C for 30 min. The solutions were then diluted 1000 times using 2% distilled superpure HNO_3 and analyzed by using ICP-MS (Thermal X Series II) using In, Rh and Re as inner standards. The standard solutions (American Lab Tech Company) were diluted to 1 μg l^{-1}, 10 μg l^{-1}, 50 μg l^{-1}, and 100 μg l^{-1} to produce the calibration curve, with linear regression coefficients all above 0.9999. The GSR-2 and GSR-22 were run as external standards to evaluate the accuracy. Analytical precision for most elements is better than 3%.

5.2. Zircon U-Pb dating

Bright and euhedral zircon grains were handpicked under a binocular microscope after conventional heavy liquid and magnetic separation, and then mounted in an epoxy resin. The sample mount was polished to expose the centers of zircons. All of the grains were photographed under transmitted and reflected light, and then examined using cathodoluminescence imaging to observe internal structures of the zircons. The U–Pb analyses of the zircons were carried using an Agilent Technologies 7700x quadrupole ICP-MS equipped with a 193 nm ArF excimer laser. The laser beam was focused on the sample with a fluency of 5.0 J/cm^2 and a spot of 40 μm diameter at a repetition rate of 5 Hz for 50 s. Helium was used as a carrier gas to transport the ablated aerosol to the mass spectrometer. Zircon Nancy 91,500 was

used as an external calibration standard to correct for instrumental mass bias and elemental fractionation (Wiedenbeck et al., 1995). Standard Mud Tank (Yuan et al., 2008) was simultaneously analyzed which yielded ages consistent with the recommended values within analytical error (Appendix Table S1). The Pb content of zircon was externally calibrated against NIST SRM 610 with Si as an internal standard, whereas other trace elements were measured with Zr as an internal standard (Hu et al., 2011). Raw-data reduction was performed off-line using the ICPMSDataCal (Liu et al., 2010). Concordia diagrams and weighted mean calculations were made using Isoplot 3.0 (Ludwig, 2003). Uncertainties on individual analyses are reported at the 1σ level, and the mean ages for pooled U-Pb analyses are quoted at 95% confidence.

5.3. Zircon Hf isotope analysis

Zircon Hf isotope analysis was carried out in situ using a Nu Instruments Nu Plasma II MC-ICP-MS equipped with a 193 nm ArF excimer laser. Analytical spots were located close to or on top of the U-Pb zircon dating spots. The analyses were conducted with a beam diameter of 50 μm, at a rate of 8 Hz, and a fluency of 6.0 J/cm^2 for 40 s. Helium was used as a carrier gas to transport the ablated aerosol to the mass spectrometer. The mass fractionations of Hf and Yb were calculated using an exponential law and values of 0.7325 for ^{179}Hf/^{177}Hf and 1.1248 for ^{173}Yb/^{171}Yb (Blichert-Toft et al., 1997). Ratios used for the corrections were ^{176}Lu/^{175}Lu = 0.02656 (Blichert-Toft et al., 1997) and ^{176}Yb/^{173}Yb = 0.7876 (McCulloch et al., 1977), respectively. To monitor the accuracy of this correction, every 5 sample analyses were followed by analysis of the reference zircons. Reference zircons GJ-1, 91500, Plešovice, Mud Tank, and Penglai were analyzed as unknowns. During the analysis, the standard zircons gave ^{176}Hf/^{177}Hf ratios consistent with recommended values (Sláma et al., 2008; Yuan et al., 2008; Li et al., 2010) within analytical error (Appendix Table S2).

The decay constant for ^{176}Lu of 1.867×10^{-11}a^{-1} was adopted (Söderlund et al., 2004) and initial ^{176}Hf/^{177}Hf ratios, denoted as $\varepsilon_{Hf}(t)$, were calculated relative to the chondritic reservoir with a ^{176}Hf/^{177}Hf ratio of 0.282772 and ^{176}Lu/^{177}Hf of 0.0332 (Blichert-Toft and Albarède, 1997). Single-stage Hf model ages (T_{DM1}) were calculated relative to the depleted mantle, which is assumed to have a linear isotopic growth from ^{176}Hf/^{177}Hf = 0.279718 at 4.55 Ga to 0.283250 at the present day with a ^{176}Lu/^{177}Hf ratio of 0.0384 (Griffin et al., 2000). Two two-stage Hf model ages (T_{DM2}) were calculated by assuming a mean ^{176}Lu/^{177}Hf value of 0.015 for the average continental crust (Griffin et al., 2002).

5.4. Muscovite ^{40}Ar/^{39}Ar dating

Muscovite grains (0.5–2 mm, and > 99% purity) were handpicked under a binocular microscope, and washed in distilled water in an ultrasonic bath, and dried. The samples were wrapped in aluminum foil and stacked in quartz vials along with the ZBH-25 biotite standard (132.7 ± 0.1 Ma at 1σ; Wang, 1983) and irradiated in the 49–2 reactor at the Beijing Atomic Energy Research Institute, with a flux of 2.65×10^{13} ncm^{-2}S^{-1} for 24 h, yielding J values of 0.004389. The irradiated samples were analyzed at the Institute of Geology, Chinese Academy of Geological Sciences. The separates were incrementally heated from 740 to 1400 °C at a rate of 40–200 °C every 10 min in the defocused beam of a 10-W CO_2 laser at increasing laser powers. The gas from each step was analyzed on a Helix MC mass spectrometer equipped with an ion-counting electron multiplier. All measurements were corrected for total system blank, mass spectrometer sensitivity, mass discrimination, radioactive decay during and subsequent to irradiation, as well as interfering Ar from atmospheric contamination and the irradiation of Ca, Cl, and K. The isotope production ratios are $(^{39}Ar/^{37}Ar_0)_{Ca} = 0.0002398$, $(^{36}Ar/^{37}Ar_0)_{Ca} = 0.000806$, and $(^{40}Ar/^{39}Ar)_K = 0.004782$. The decay constant for ^{40}K used in the calculation was 5.543×10^{-10} y^{-1} (Steiger and Jäger, 1977). The ^{40}Ar/^{39}Ar results were calculated and plotted using Isoplot 3.0 (Ludwig, 2003). Plateau ages are considered here when three or more consecutive steps release more than 50% of the ^{39}Ar and their respective errors overlap at the 1σ level.

6. Results

The major and trace element compositions of the granite porphyry are provided in Table 1. For comparative purposes when discussing the data, we have also included on the figures published data for the Cenozoic granitic porphyries related to porphyry copper deposits (PCD)

Table 1
Major and trace element compositions of granite porphyry from the Siruyidie'er prospect.

Sample	X4-1	X4-2	X4-3	X4-4	X4-5	Sample	X4-1	X4-2	X4-3	X4-4	X4-5
SiO_2	69.70	69.06	70.05	70.05	69.99	Ba	3231.41	2985.83	3247.20	3142.93	3316.25
TiO_2	0.34	0.35	0.35	0.32	0.35	La	100.55	105.23	107.00	116.60	105.71
Al_2O_3	14.65	15.09	14.81	14.44	14.65	Ce	152.71	157.33	162.47	176.05	158.71
TFe_2O_3	1.62	1.51	1.61	1.66	1.62	Pr	11.82	12.18	12.95	13.68	12.31
MnO	0.01	0.02	0.01	0.02	0.01	Nd	41.33	42.76	43.03	44.78	43.38
MgO	0.63	0.56	0.61	0.54	0.63	Sm	5.17	5.15	5.55	5.90	5.40
CaO	0.80	0.87	0.82	0.87	0.80	Eu	1.38	1.31	1.47	1.41	1.43
Na_2O	3.16	3.52	3.27	3.81	3.15	Gd	4.19	4.24	4.47	4.66	4.34
K_2O	6.03	6.03	6.07	6.46	6.04	Tb	0.47	0.46	0.50	0.52	0.50
P_2O_5	0.09	0.10	0.10	0.08	0.10	Dy	1.79	1.62	1.80	1.77	1.94
LOI	2.04	2.43	2.10	1.71	2.05	Ho	0.36	0.31	0.35	0.34	0.39
Mg#	43.63	42.56	43.03	39.04	43.31	Er	1.13	1.04	1.15	1.11	1.21
A/NK	1.25	1.22	1.24	1.09	1.25	Tm	0.19	0.17	0.19	0.17	0.21
A/CNK	1.11	1.08	1.10	0.97	1.11	Yb	1.25	1.14	1.25	1.20	1.35
Sc	4.21	4.29	4.34	4.45	4.31	Lu	0.20	0.19	0.20	0.19	0.22
V	25.10	27.04	24.47	23.88	21.33	Hf	5.51	5.35	5.20	5.47	5.47
Cr	6.74	6.84	6.73	6.88	8.28	Ta	0.58	0.60	0.60	0.64	0.59
Co	0.78	1.05	0.90	1.00	1.00	Pb	19.06	16.94	18.98	17.63	19.80
Rb	204.26	207.47	209.12	216.64	209.79	Th	48.81	50.89	50.89	53.68	50.98
Sr	370.35	311.21	358.43	322.49	378.34	U	6.43	6.45	6.58	6.74	6.67
Y	9.21	7.88	8.83	8.39	9.91	Sr/Y	40.22	39.50	40.60	38.45	38.18
Zr	235.85	227.24	208.45	222.30	231.39	ΣREE	322.53	333.11	342.39	368.36	337.11
Nb	9.73	10.41	10.22	10.57	9.96	Eu/Eu*	0.87	0.83	0.87	0.79	0.87

Note: Mg# = $Mg^{2+}/(Mg^{2+} + Fe^{2+})$ (molar ratio); A/CNK = $Al_2O_3/(CaO + Na_2O + K_2O)$ (molar ratio); A/NK = $Al_2O_3/(Na_2O + K_2O)$ (molar ratio). Eu/Eu* = $2Eu_N/(Sm_N + Gd_N)$.

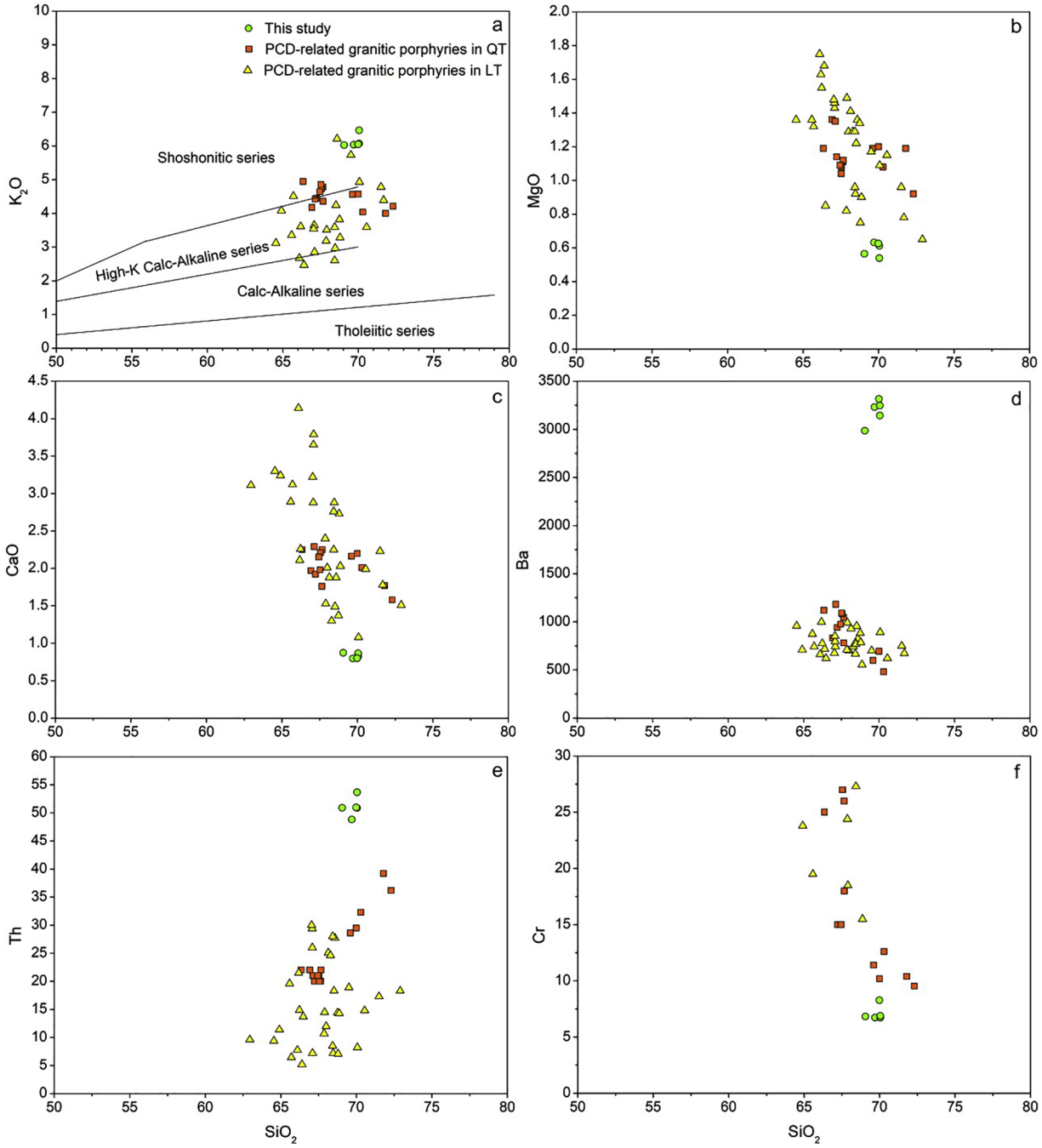

Fig. 7. Plots of selected major and trace elements versus SiO_2 for granite porphyry from Siruyidie'er prospect and for Eocene to Miocene PCD-related granitic porphyries from Qiangtang and Lhasa terranes (data sourced from Hou et al., 2015a,b; Jiang et al., 2006; Yang et al., 2016; Yang et al., 2014). (a) KO_2 versus SiO_2 classification diagram (Peccerillo and Taylor, 1976); (b-f) Plot of MgO, CaO, Ba, Th, and Cr versus SiO_2.

from the Qiangtang and Lhasa terranes.

The granite porphyry samples are silica-saturated with high abundances of SiO_2 (69.06–70.05 wt%) and total alkalis ($K_2O + Na_2O$ = 9.17–10.27 wt%). They are shoshonite rocks with K_2O/Na_2O ratios range from 1.70 to 1.92 (Fig. 7a). They are low in MgO, total Fe_2O_3, P_2O_5, Yb, Ta, Cr, and Ni, very low in V (21–27 ppm), Y (7.9–9.9 ppm), and HREE (4.9–5.8 ppm), and rich in Rb (204–217 ppm), Ba (2986–3316 ppm), Th (49–54 ppm), and LREE (317–363 ppm) contents (Fig. 7b-7f). In addition, they exhibit high Sr/Y ratios (38–41) (Fig. 8a). In the chondrite-normalized REE diagram, the rocks are characterized by enrichment of LREE (La_N/Yb_N = 55–66), and display slight HREE fractionation (Gd_N/Yb_N = 2.6–3.1) with slightly to moderate negative Eu anomalies (δEu = 0.79–0.87) (Fig. 9a). In the primitive mantle-normalized trace element diagram, the granite porphyry exhibits relative enrichment in LILEs (e.g., Ba, Rb, K), LREEs, and Zr and Hf, and depletion in HFSEs (e.g., Th, U, Nb, Ta, Ti, and Y), P, and Sr (Fig. 9b).

Compared to the Cenozoic PCD-related granitic porphyries from the Qiangtang and Lhasa terranes (Figs. 7 and 8), the granite porphyry has much higher Ba and LREEs contents, high K_2O and Th contents, but lower CaO, MgO, Fe_2O_3, P_2O_5, V, and Ci contents, and Sr/Y ratios. Compared with primitive mantle compositions, all the granitic porphyries display a similar enrichment of LILEs over HFSEs but the samples from the Siruyidie'er prospect are highly enriched in Ba and depleted in Sr (Fig. 9).

U-Pb ages of 20 zircon grains from the granite porphyry were

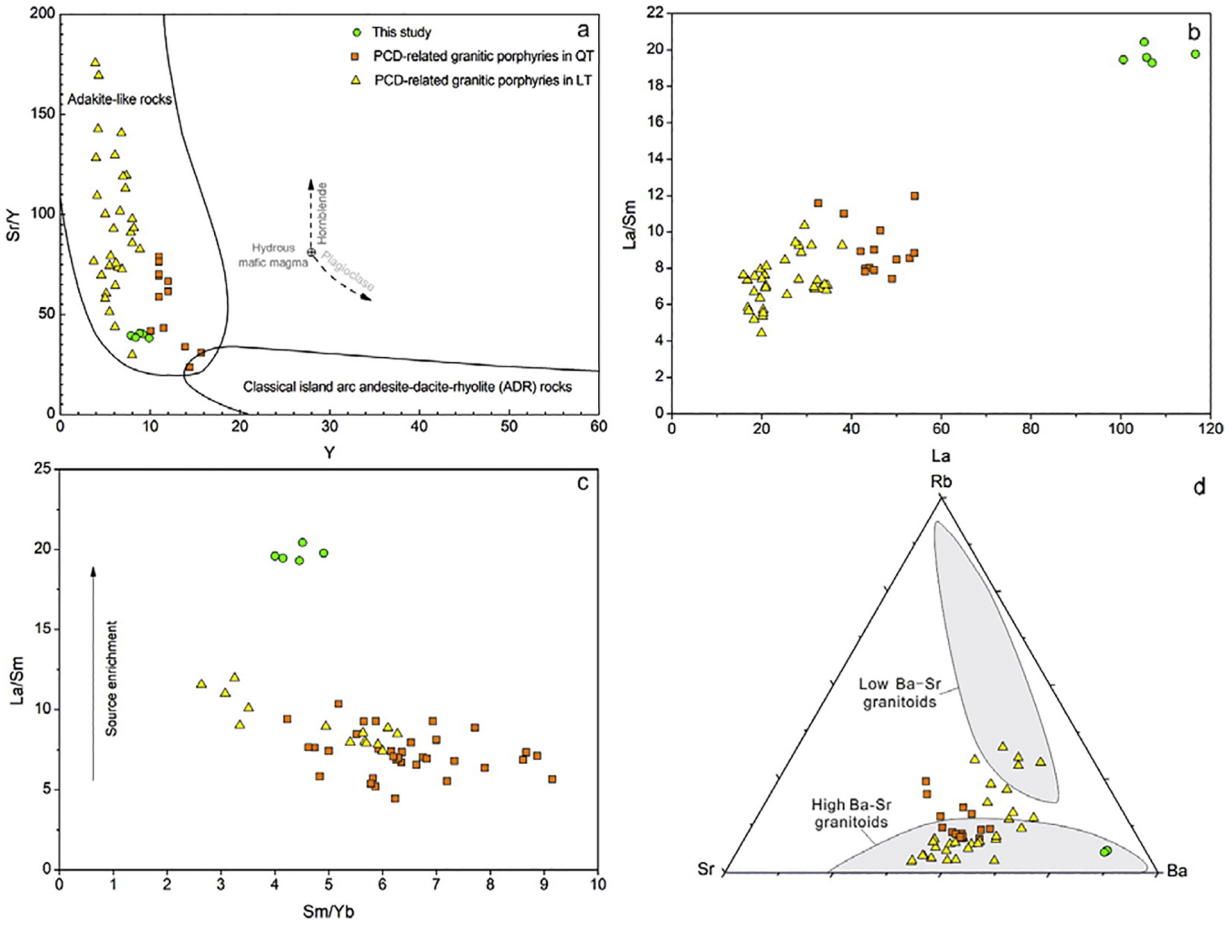

Fig. 8. (a) Plot of Sr/Y versus Y. Fields for adakites and classical island arc magmatic rocks are from Defant and Drummond (1990); (b) Plot of La/Sm versus La; (c) Plot of La/Sm versus Sm/Yb; (d) Sr–Rb–Ba plot. Fields of high Ba–Sr and low Ba–Sr granitoids are based on data from Tarney and Jones (1994). Data sources are as in Fig. 6.

obtained (Table 2). The zircon grains have a size of 90–220 μm with length/width ratios of 1:1–3:1 and show oscillatory zoning in cathodoluminescence (CL) images (Fig. 10a), indicating a magmatic origin. The grains have U and Th concentrations ranging from 690 to 1909 and from 289 to 1463 ppm, respectively, corresponding to Th/U values of 0.41 to 0.77. Individual grains yield similar $^{206}Pb/^{238}U$ ages ranging from 13.7 to 13.8 Ma, with a weighted mean age of 13.74 ± 0.21 Ma (Fig. 11a), which is interpreted as the crystallization age of the granite porphyry. Zircons from the magmatic breccia are typically small (50–150 μm) and have complex textures, including oscillatory zoning, flat-CL response, metamict zone, and core-rim texture (Fig. 10b). Individual grains yield dates between 205 Ma and 13 Ma (Table 2, Fig. 11b).

Lutetium-Hf isotope data were obtained for 20 grains of the dated zircons and the data are given in Table 3 and plotted in Fig. 12. The zircon grains have initial $^{176}Hf/^{177}Hf$ ratios of 0.282515–0.282622 and $\varepsilon_{Hf}(t)$ values of −8.78 to −5.01, calculated at 13.74 Ma, contrasting with other reported $\varepsilon_{Hf}(t)$ values of Cenozoic granitoids that related to the mineralization of porphyry Cu ± Mo ± Au deposits in Tibetan plateau. Their two-stage depleted mantle model ages (T_{DM2}) range from 1410 to 1648 Ma.

The $^{40}Ar/^{39}Ar$ results of hydrothermal muscovite are summarized in Table 4 and the age spectra are depicted in Fig. 13. The ^{39}Ar release profile shows a slight disturbance in the low-temperature steps, leading to older apparent ages, but produced a weighted mean plateau age of 13.68 ± 0.17 Ma between steps 6 and 10 (Fig. 13a), accounting for 76.7% of the ^{39}Ar released. The inverse isochron plot yielded the same age of 13.34 ± 0.88 Ma but shows a low degree of concordancy (MSWD = 20). The initial $^{40}Ar/^{36}Ar$ ratio (306) (Fig. 13b) is slightly higher than atmospheric (the recommended value is 295.5), demonstrating that negligible excess argon was released between steps 6 and 10.

7. Discussion

7.1. Timing of mineralization at Siruyidie'er prospect and genetic implications

Hydrothermal muscovite from No. I prospect is intergrown with pyrite, fluorite and epidote within fissures of altered porphyritic granite (Fig. 7e–f), it can be considered to have formed synchronously with the mineralizing event at Siruyidie'er prospect. Based on this field observation, the $^{40}Ar/^{39}Ar$ data from No. I prospect demonstrate that hydrothermal activity and mineralization at Siruyidie'er prospect probably occurred at 13.34 ± 0.88 Ma (Fig. 13).

A deep drill hole (zk0-1; Fig. 2b, Fig. 3) in the Siruyidie'er block has revealed that Mo and Cu mineralization, and widespread pyrite-fluorite-chlorite alteration and magmatic and hydrothermal breccias likely formed by the eruption of felsic magma and hydrothermal fluids triggered by the granite porphyry at depth. In the Geierdikele block, field relationships show that significant copper mineralization has a spatial association with the granite porphyry (Fig. 6a–d). These field evidences suggest that Mo and Cu mineralization and brecciation at Siruyidie'er prospect have close spatial, temporal and genetic links to the granite porphyry, which is further supported by the precise geochronological data. Zircon grains from the granite porphyry and

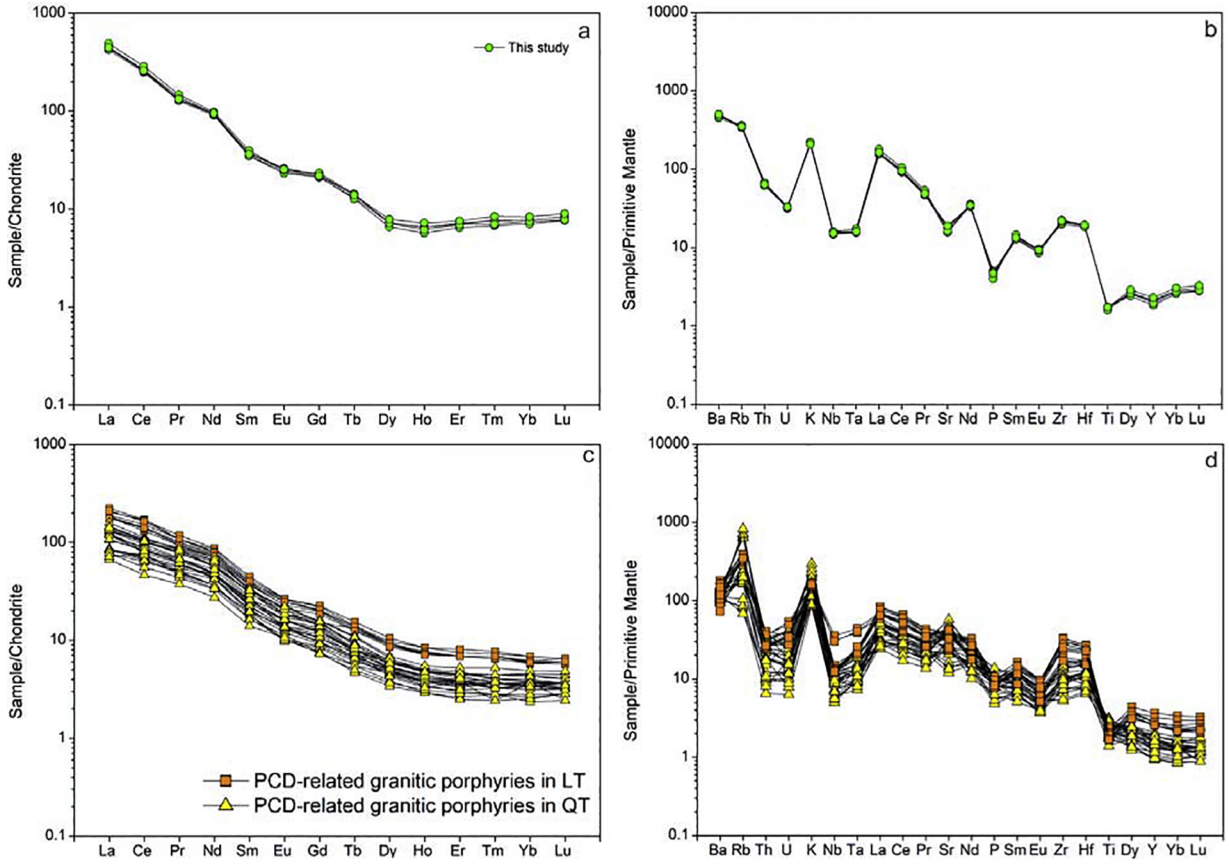

Fig. 9. Chondrite-normalized REE and primitive mantle-normalized multi-element diagrams for (a-b) granite porphyry from Siruyidie'er prospect and for (c-d) Eocene to Miocene PCD-related granitic porphyries from Qiangtang and Lhasa terranes. Chondrite- and primitive mantle-normalization values are from Sun and McDonough (1989). Data sources are as in Fig. 6.

magmatic breccia yield a weighted $^{206}Pb/^{238}U$ mean age of 13.74 ± 0.21 Ma and a youngest $^{206}Pb/^{238}U$ age of 13.70 ± 0.70 Ma, respectively. These ages are in good agreement with the 13.34 ± 0.88 Ma $^{40}Ar/^{39}Ar$ plateau age determined for hydrothermal muscovite, suggesting synchronism of the hydrothermal Mo- and Cu-bearing episode and this magmatic event.

The most prominent characteristic of the Siruyidie'er prospect is the development of 14 magmatic-hydrothermal breccia pipes (Fig. 2). Magmatic-hydrothermal breccia is the products of the release of over-pressured magmatic fluids (Sillitoe, 1985). Many porphyry deposits contain more or less volumes of magmatic-hydrothermal breccia (Sillitoe, 2010). Examples include the porphyry Cu-Mo-Au deposit at Agua Rica, Argentina (Landtwing, 2002), the porphyry Cu-Au deposit at Galore Creek, British Columbia (Byrne and Tosdal, 2014), the porphyry Mo deposit at Questa, New Mexico (Ross et al., 2002), the porphyry Au deposit at Qiyugou (Chen et al., 2009), China, and the porphyry Cu-Mo deposit at Río Blanco-Los Bronces, Chile (Frikken et al., 2005). Breccias in these deposits, occupying steep, pipe-like to irregular bodies, are intermineral in timing as a result of being generated in close association with ore-related porphyry (Landtwing, 2002; Ross et al., 2002; Frikken et al., 2005), which is similar with field and age evidences at Siruyidie'er prospect. Together with the data from geology and geochronology results, we propose that the Siruyidie'er prospect is a porphyry deposit related to a Miocene magmatic-hydrothermal system.

7.2. Magma source of the granite porphyry

The granite porphyry at Siruyidie'er prospect has geochemical features that are similar to most modern subduction-related magmatic rocks, including enrichment of LREE and LILEs, and depletion of HREE, HFSEs, Nb, Ta, and Ti (Fig. 9a–b). These features indicate that the magma source of the granite porphyry may experience subduction-related fluid or melt metasomatism before partial fusion. However, compared to arc magmatic rocks, the granite porphyry at Siruyidie'er prospect has higher K contents (6.03–6.46 wt%). Furthermore, although the Cenozoic post-collisional high-K magmatic rocks in the Tibetan plateau show a similar geochemical feature with the granite porphyry at Siruyidie'er prospect, including high K contents and subduction signatures (Liu et al., 2014), the latter has a conspicuously higher Ba content (2985–3316 ppm). This implies that the granite porphyry at Siruyidie'er prospect may have a different magma source different from those of the arc magmatic rocks and post-collisional shoshonite to high-K magmatic rocks in the Tibetan plateau.

On the Rb-Ba-Sr plot, the granite porphyry in this study plots in the high Ba-Sr granite field (Fig. 8d). The high Ba, Sr, and K/Rb with low Rb, Th, U, Nb, Y, and HREE with negligible Eu anomaly of the granite porphyry also consistent with the high Ba-Sr granite that was proposed by (Tarney and Jones, 1994). Former studies show that there are many possible sources and/or petrogenesis of the high Ba-Sr granite, e.g., the partial melting of underplated mafic rocks (Tarney and Jones, 1994; Mahéo et al., 2009), lithospheric mantle that had been metasomatized by asthenosphere-derived carbonatitic melts (Tarney and Jones, 1994) or subduction-related fluids (Jiang et al., 2012; Peng et al., 2013), subducted ocean islands or ocean plateaus (Tarney and Jones, 1994), or lower mafic continental crust and/or "enriched" crustal source (Lara et al., 2017).

The low Rb and high Ba and Sr contents of the granite porphyry combined with the negligible Eu anomaly of the granite porphyry suggest that the granite porphyry are not highly evolved and that fractional crystallization of feldspars was not an important process

Table 2
LA-ICP-MS U-Pb zircon analytical data of granite porphyry and magmatic breccia from the Siruyidie'er prospect.

Spot No.	Contents			Th/U	Corrected Ratios						Corrected Ages (Ma)					
	Pb	Th	U		207Pb/206Pb Ratio	207Pb/206Pb ± 1σ	207Pb/235U Ratio	207Pb/235U ± 1σ	206Pb/238U Ratio	206Pb/238U ± 1σ	207Pb/206Pb Age	207Pb/206Pb ± 1σ	207Pb/235U Age	207Pb/235U ± 1σ	206Pb/238U Age	206Pb/238U ± 1σ
	ppm															
Granite porphyry																
X-4-1	3.29	684	1299	0.53	0.0478	0.0065	0.0138	0.0017	0.0021	0.0001	100	289	13.9	1.7	13.8	0.5
X-4-2	2.65	500	1056	0.47	0.0469	0.0093	0.0137	0.0022	0.0021	0.0001	55.7	406	13.8	2.2	13.8	0.5
X-4-3	2.90	507	1126	0.45	0.0491	0.0089	0.0134	0.0020	0.0021	0.0001	154	374	13.6	2.0	13.8	0.5
X-4-4	3.23	514	1266	0.41	0.0476	0.0070	0.0137	0.0016	0.0021	0.0001	76.0	318	13.8	1.6	13.8	0.5
X-4-5	4.02	879	1488	0.59	0.0476	0.0073	0.0137	0.0018	0.0021	0.0001	76.0	330	13.8	1.8	13.7	0.4
X-4-6	2.95	569	1149	0.50	0.0572	0.0160	0.0136	0.0029	0.0021	0.0001	502	519	13.7	2.9	13.7	0.7
X-4-7	3.30	672	1276	0.53	0.0492	0.0065	0.0136	0.0016	0.0021	0.0001	167	272	13.7	1.6	13.7	0.4
X-4-8	2.48	469	934	0.50	0.0540	0.0090	0.0141	0.0022	0.0021	0.0001	369	341	14.2	2.2	13.8	0.6
X-4–9	3.22	704	1204	0.58	0.0593	0.0151	0.0137	0.0017	0.0021	0.0001	576	474	13.8	1.7	13.7	0.4
X-4-10	3.27	714	1228	0.58	0.0490	0.0062	0.0139	0.0013	0.0021	0.0001	146	274	14.0	1.3	13.7	0.4
X-4-11	2.63	482	1007	0.48	0.0496	0.0076	0.0136	0.0013	0.0021	0.0001	176	326	13.7	1.3	13.8	0.5
X-4-12	5.20	1463	1909	0.77	0.0488	0.0059	0.0138	0.0013	0.0021	0.0001	139	259	13.9	1.3	13.7	0.4
X-4-13	4.11	1057	1508	0.70	0.0533	0.0138	0.0135	0.0029	0.0021	0.0001	343	500	13.7	2.9	13.8	0.8
X-4-14	3.04	563	1172	0.48	0.0510	0.0092	0.0134	0.0017	0.0021	0.0001	243	367	13.6	1.7	13.7	0.4
X-4-15	3.80	748	1432	0.52	0.0466	0.0055	0.0139	0.0014	0.0021	0.0001	27.9	272	14.0	1.4	13.8	0.4
X-4-16	3.07	541	1184	0.46	0.0488	0.0092	0.0137	0.0020	0.0021	0.0001	200	331	13.8	2.0	13.7	0.5
X-4-17	1.96	341	752	0.45	0.0527	0.0152	0.0138	0.0029	0.0021	0.0001	322	543	14.0	2.9	13.7	0.8
X-4-18	1.76	289	690	0.42	0.0691	0.0198	0.0138	0.0020	0.0021	0.0001	902	625	13.9	2.0	13.7	0.7
X-4-19	3.09	573	1213	0.47	0.0468	0.0059	0.0135	0.0014	0.0021	0.0001	39.0	281	13.7	1.4	13.8	0.4
X-4-20	3.57	745	1330	0.56	0.0507	0.0112	0.0142	0.0022	0.0021	0.0001	228	444	14.3	2.2	13.8	0.7
Magmatic breccia																
JL-5-1-1	36.0	416	1816	0.23	0.0483	0.0041	0.1241	0.0104	0.0186	0.0003	122	180	119	9.4	119	2.2
JL-5-1-2	7.26	1519	2509	0.61	0.0576	0.0148	0.0136	0.0032	0.0021	0.0001	522	476	13.7	3.2	13.7	0.7
JL-5-1-3	151	686	5031	0.14	0.0500	0.0038	0.2139	0.0160	0.0307	0.0005	195	−19	197	13.4	195	3.1
JL-5-1-4	170	2110	4801	0.44	0.0529	0.0025	0.2193	0.0104	0.0298	0.0005	328	109	201	8.7	189	3.1
JL-5-1-5	157	2595	3842	0.68	0.0523	0.0033	0.2240	0.0145	0.0308	0.0005	298	144	205	12.0	196	3.3
JL-5-1-6	129	904	3912	0.23	0.0494	0.0020	0.2171	0.0088	0.0317	0.0004	169	92	199	7.4	201	2.4
JL-5-1-7	163	923	5496	0.17	0.0515	0.0022	0.2204	0.0096	0.0310	0.0006	265	101	202	8.0	197	3.6
JL-5-1-8	243	2068	7380	0.28	0.0518	0.0019	0.2223	0.0085	0.0311	0.0003	276	90	204	7.1	197	2.0

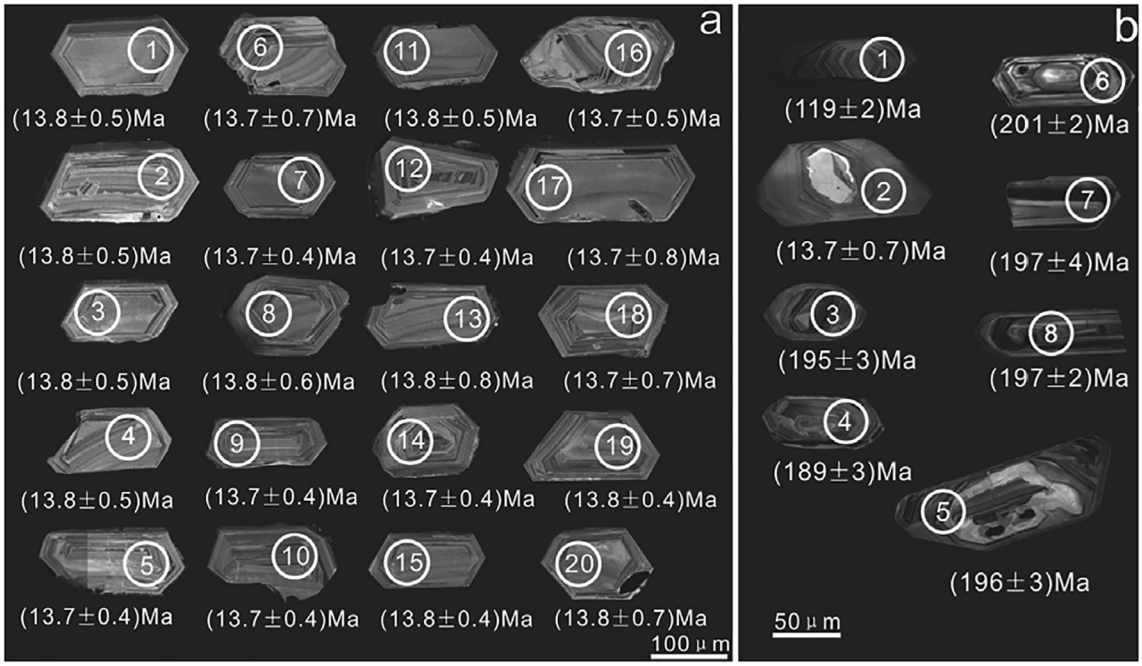

Fig. 10. (a) Cathodoluminescence (CL) images of zircon grains from granite porphyry; (b) CL images of zircon grains from magmatic breccia. White circles are analyzed spots and U-Pb dates (Ma).

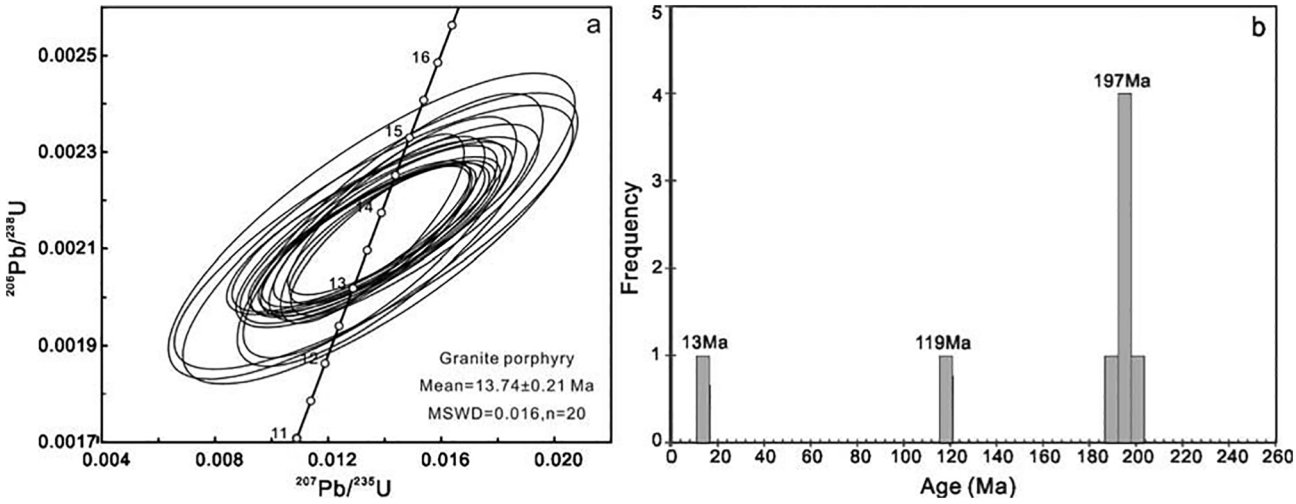

Fig. 11. (a) U–Pb concordia diagram for zircons from granite porphyry; (b) Histograms of U-Pb zircon date for magmatic breccia.

(Miller et al., 1999). Fractionation from mantle-derived appinitic magmas or magma mingling which is common in the genesis of felsic high Ba-Sr granitoids (Tarney and Jones, 1994; Fowler et al., 2008) can be precluded as field evidence of the interaction between basic to acid granitic magmas in the granite porphyry is scarce. The granite porphyry has lower LREE concentrations than those of coeval mantle-derived syenite (Jiang et al., 2012) in the Taxkorgan complex also do not support an origin from mantle-derived magma by fractional crystallization processes. The granite porphyry at Siruyidie'er prospect is characterized by high SiO_2, K_2O, and K_2O/Na_2O ratio, and low MgO and Cr (6.73–8.28 ppm) concentrations. These features indicate a crustal source. The $\varepsilon_{Hf}(t)$ of the zircon grains from the granite porphyry are all lower than 0 epsilon (–8.78 to −5.01) with T_{DM2} ages range from 1410 to 1648 Ma, confirming that the granite porphyry magmas could be derived predominantly from continental crust.

The remaining question is the nature of the continental crust that the granite porphyry magma sourced. Partial melting of tholeiitic, calc-alkaline, and alkaline basaltic amphibolites in the lower crust can be excluded as experimental studies indicate that these protoliths generally have K_2O contents too low to allow evolution into the high-K_2O field (Xiao and Clemens, 2007). The granite porphyry is characterized by highly fractionated REE patterns, very low HREE contents, and slightly negative Eu anomalous. Partial melting of overthickened lower crust with a residue of garnet but plagioclase-free can account for these patterns (Miller et al., 1999); nonetheless, it is also difficult to explain the K-rich character of the granite porphyry. Experimental studies demonstrated that partial melting of typical crustal rocks or metasediments, at pressures higher than crustal pressures (equal to granulate and/or eclogite faces), can produces high-K melts and the K_2O/Na_2O ratios in the melts increase with increasing temperature and pressure (Hermann and Spandler, 2007). Hence, the geochemical characteristics of the granite porphyry from the Siruyidie'er prospect can be explained by high degrees of partial melting of crustal sedimentary rocks under granulite and/or eclogite conditions. Additional evidence includes: 1) block of continental crust consists of sediments, e.g., pelite, has pushed into the upper mantle depth beneath the Pamir (Ducea et al., 2003; Hacker et al., 2005; Kooijman et al., 2017); 2) the protoliths of the eclogite and granulite xenoliths from the Pamir are partially consist of sediments(Hacker et al., 2005); 3) the source depth of the Tasikuergan complex, inferred by Jiang et al.(2012), is 70–100 km; 4) the weakly negative Eu anomalies in the trace element patterns of the granite porphyry, which indicate the absence of plagioclase in restite, which in

Table 3
In-situ zircon Hf isotopic data of granite porphyry from the Siruyidie'er prospect.

Spot No.	$^{176}Lu/^{177}Hf$	2σ	$^{176}Yb/^{177}Hf$	2σ	$^{176}Hf/^{177}Hf$	2σ	Age	$^{176}Hf/^{177}Hf(t)$	$\varepsilon_{Hf}(t)$	T_{DM} (Ma)	T_{2DM} (Ma)
X-4-1	0.000519	0.000003	0.014121	0.000159	0.282566	0.000011	13.74	0.282565	−7.01	959	1536
X-4-2	0.000466	0.000003	0.013078	0.000147	0.282575	0.000012	13.74	0.282575	−6.66	944	1514
X-4-3	0.000516	0.000003	0.016326	0.000108	0.282573	0.000010	13.74	0.282573	−6.73	948	1519
X-4-4	0.000553	0.000002	0.014705	0.000068	0.282546	0.000010	13.74	0.282546	−7.71	988	1580
X-4-5	0.000539	0.000002	0.014070	0.000084	0.282575	0.000009	13.74	0.282575	−6.66	946	1514
X-4-6	0.000526	0.000003	0.017308	0.000186	0.282582	0.000011	13.74	0.282581	−6.44	937	1500
X-4-7	0.000535	0.000004	0.014252	0.000100	0.282558	0.000009	13.74	0.282558	−7.28	970	1553
X-4-8	0.000484	0.000003	0.016068	0.000127	0.282581	0.000012	13.74	0.282581	−6.45	937	1501
X-4-9	0.000524	0.000005	0.015300	0.000173	0.282554	0.000009	13.74	0.282553	−7.43	976	1563
X-4-10	0.000642	0.000001	0.017887	0.000063	0.282622	0.000009	13.74	0.282622	−5.01	883	1410
X-4-11	0.000502	0.000002	0.014667	0.000089	0.282576	0.000009	13.74	0.282575	−6.65	945	1514
X-4-12	0.000687	0.000006	0.023123	0.000196	0.282515	0.000009	13.74	0.282515	−8.78	1033	1648
X-4-13	0.000580	0.000002	0.015000	0.000060	0.282572	0.000008	13.74	0.282572	−6.79	952	1522
X-4-14	0.000478	0.000002	0.015514	0.000120	0.282578	0.000009	13.74	0.282577	−6.58	941	1509
X-4-15	0.000639	0.000003	0.017250	0.000086	0.282569	0.000009	13.74	0.282569	−6.88	957	1528
X-4-16	0.000544	0.000003	0.014670	0.000099	0.282548	0.000008	13.74	0.282548	−7.64	985	1576
X-4-17	0.000359	0.000005	0.010561	0.000171	0.282555	0.000010	13.74	0.282555	−7.38	970	1560
X-4-18	0.000485	0.000002	0.013795	0.000048	0.282551	0.000009	13.74	0.282551	−7.51	978	1567
X-4-19	0.000491	0.000002	0.013068	0.000049	0.282539	0.000012	13.74	0.282539	−7.94	995	1595
X-4-20	0.000566	0.000003	0.017555	0.000063	0.282564	0.000011	13.74	0.282564	−7.06	962	1539

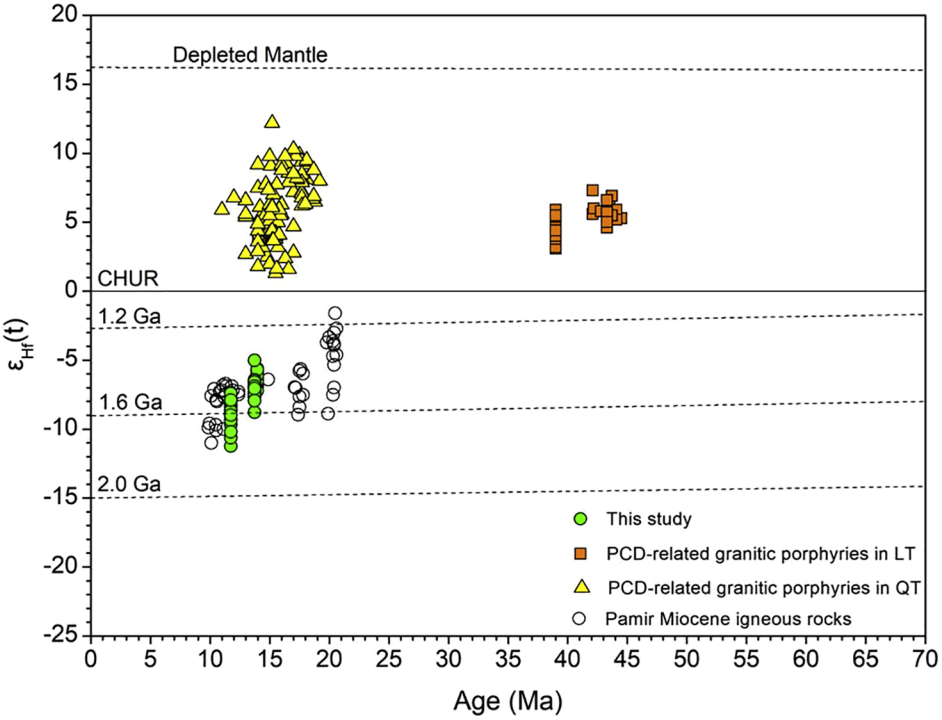

Fig. 12. New and compiled zircon $\varepsilon_{Hf}(t)$ data plotted against zircon U–Pb ages. Isotopic data for Pamir Miocene igneous rocks come from Chapman et al. (2018) and Jiang et al. (2012). The other data sources are as in Fig. 6.

turn requires melting under eclogite or granulite facies conditions.

7.3. Comparison with PCD in the Tibetan plateau between magmatic series and its metallogenic implications

Our mineralization age data shows that Cu-bearing mineralization at Siruyidie'er prospect was contemporaneous with a period of crustal extension and with voluminous magmatism in the Pamir-Tibetan plateau in a post-collisional extensional setting related to the India-Asian continent collision (Chapman et al., 2018). Although the Siruyidie'er prospect is the only case of porphyry deposit recognized in the Central Pamir till now, large-scale Oligocene to Miocene porphyry Cu ± Mo ± Au deposits are present in the Tibetan plateau (Fig. 1), including the eastern Qiangtang and south Lhasa terranes. Similar with the Siruyidie'er, these Cu ± Mo ± Au deposits were all formed in a post-collisional extensional setting related to the break-off of the Neo-Tethyan slab (Negredo et al., 2007; Smit et al., 2014; Stearns et al., 2015) or rollback and break-off of the Indian plate (Ding et al., 2005; Kapp et al., 2007; DeCelles et al., 2011) during the Oligocene to Miocene times. Typical cases of porphyry deposits within the Tibetan plateau include the Yulong, Duoxiaosongduo, Malasongduo, and Narigongma Cu ± Mo deposits in the Qiangtang terrane (Jiang et al., 2006; Yang et al., 2009; Yang et al., 2014; Hou and Zhang, 2015), and the Qulong, Jiama, Nanmu, Jiru, Zhunuo, Tinggong, Chongjiang, Bairong, and Tangbula Cu ± Mo ± Au deposits in the south Lhasa terrane (Hou et al., 2009; Hou et al., 2015a; Hou et al., 2015b; Yang et al., 2016).

The preceding texts have indicated that the geology and mineralization at the Siruyidie'er prospect are akin to those of porphyry deposit. Moreover, the Siruyidie'er prospect evidently formed contemporaneously with numerous PCD deposits in the Lhasa terrane. The question is: does the Siruyidie'er prospect has the potential to form large-scale porphyry Cu ± Mo ± Au deposits? To answer this question, we have selected published geochemical data for the Oligocene to

Table 4
$^{40}Ar/^{39}Ar$ data of hydrothermal muscovite from the Siruyidie'er prospect.

Step	T (°C)	$^{40}Ar/^{39}Ar$	$^{37}Ar/^{39}Ar$	$^{36}Ar/^{39}Ar$	$^{38}Ar/^{39}Ar$	$^{40}Ar^{*}/^{39}Ar_{K}$	$^{40}Ar^{*}$(%)	$^{39}Ar_{K}$(%)	Apparent age (Ma)	± 1 σ (Ma)
J value = 0.004389 ± 0.0000135										
1	680	314.94	0.00	1.0347	0.1870	9.1875	2.92	0.13	74.00	19.00
2	740	16.07	0.00	0.0484	0.0191	1.7540	10.91	1.38	14.41	0.80
3	780	8.99	0.00	0.0229	0.0153	2.2204	24.71	3.37	18.23	0.76
4	820	14.98	0.00	0.0431	0.0217	2.2368	14.93	5.96	18.36	0.20
5	860	6.14	0.00	0.0135	0.0128	2.1541	35.07	10.93	17.68	0.32
6	900	4.25	0.00	0.0086	0.0161	1.7000	39.96	22.05	13.97	0.17
7	940	2.69	0.00	0.0033	0.0034	1.6911	62.97	28.88	13.90	0.21
8	980	2.24	0.00	0.0021	0.0135	1.6124	72.03	55.88	13.25	0.14
9	1040	2.71	0.00	0.0032	0.0071	1.7516	64.73	58.87	14.39	0.42
10	1100	2.43	0.00	0.0025	0.0132	1.6837	69.33	87.59	13.84	0.15
11	1200	5.17	0.00	0.0097	0.0128	2.3009	44.54	95.92	18.89	0.24
12	1400	7.11	0.00	0.0156	0.0191	2.4872	35.00	100.00	20.40	0.44

Note: The terms $^{40}Ar^{*}$ and $^{39}Ar_{K}$ denote radiogenic ^{40}Ar and nucleogenic ^{39}Ar, respectively.

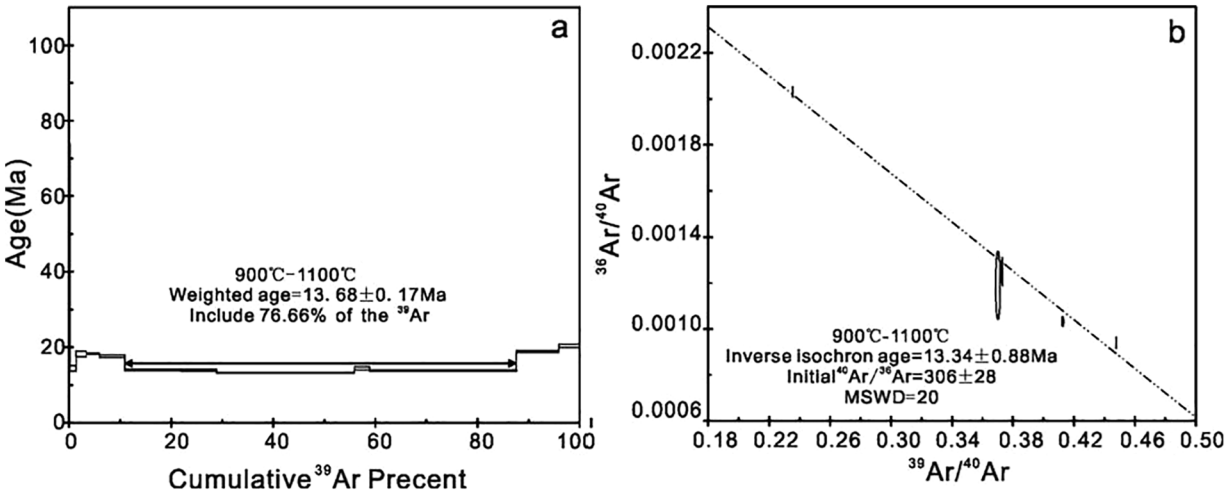

Fig. 13. (a) Laser-heated $^{40}Ar/^{39}Ar$ age spectra of ore-related muscovite from Siruyidie'er prospect; (b) The $^{39}Ar/^{40}Ar$-$^{36}Ar/^{40}Ar$ inverse isochron correlation diagram of ore-related muscovite from Siruyidie'er prospect.

Miocene granitic porphyries related to PCD from the Qiangtang and Lhasa terranes for comparison study.

Comparison of the ore-forming granitic porphyries shows significant differences that may reflect variations in sources of magma generation. These differences include the types of phenocryst assemblages and compositions of the magmas. Granite porphyry at Siruyidie'er prospect commonly contains quartz and K- feldspar phenocrysts. Phenocrysts of hydrous minerals, e.g., biotite or hornblende, are absent in this rock, suggesting low magmatic water contents (≤3 wt%) (Candela, 1997). Porphyries from the PCD in the Qiangtang and Lhasa terranes contain abundant phenocrysts of hydrous minerals (Hou et al., 2006; Jiang et al., 2006; Wang et al., 2014; Yang et al., 2014; Hou and Zhang, 2015; Yang et al., 2016), e.g., hornblende and biotite, as well as plagioclase, and clino- and ortho-pyroxenes, suggesting high magmatic water contents.

Comparisons of the chemical composition of ore-forming granitic porphyries from the Pamir and Tibetan plateaus highlight systematic differences between them (Figs. 7–9). The granitic porphyries from the Tibetan plateau are high-K calc-alkaline series. They are noteworthy for their high MgO, CaO, Fe_2O_3, P_2O_5, Cr, and Sr contents. These rocks are enriched in LILEs (Ba, Rb, K) and LREEs, and depleted in HFSEs (Th, U, Nb, Ta, Ti, and Y), and they have high Sr/Y ratios. Compositional characteristics of this assemblage indicate that melting was enhanced by volatile flux from the subducting plate, resulting in oxidized, water-rich magmas enriched in K, Rb, Sr, and Ba relative to high field strength elements (Richards et al., 2012; Richards, 2015). Hf isotopic data indicate that rocks of the Tibetan plateau were generated by partial melting of underplated juvenile mafic rocks or the depleted mantle wedge above subducting oceanic lithosphere of the India plate (Fig. 12) (Jiang et al., 2006; Richards, 2009; Hou et al., 2015b). In contrast, porphyry at the Siruyidie'er prospect has lower CaO, MgO, Fe_2O_3, P_2O_5, and Ci contents, and Sr/Y ratios. They are enriched in LILEs and LREEs, and depleted in HFSEs, but are highly enriched in LREEs, Ba, and K_2O, and have relatively high La/Sm and Ba/Nb ratios. Zircon Hf isotopic data indicate that the silicic rocks probably were produced by partial melting of the ancient continental crust.

As discussed above, magmas of the Tibetan plateau were relatively water-rich and oxidized, which are characteristics typical of porphyry Cu ± Mo ± Au deposits throughout the world. In contrast, magmas of the granite porphyry at Siruyidie'er prospect had lower water contents (indicated by lacking of hydrous minerals of hornblende and biotite) and possibly lower oxygen fugacity (indicated by the occurrences of ilmenite), and silicic magmas were derived from ancient crustal materials. These magmas can be affiliated with Mo-rich porphyry systems (Richards, 2015; Sun et al., 2015). It means that the Siruyidie'er prospect has a potential to form porphyry Mo ± Cu but not porphyry Cu ± Mo ± Au deposit. Breccia pipes from the Siruyidie'er block contain abundant fluorites support this assumption.

8. Conclusion

Field and petrologic evidence establish a genetic link of the Siruyidie'er prospect with granite porphyry intrusion. Zircon grains from the granite porphyry show weighted $^{206}Pb/^{238}U$ mean age of 13.74 ± 0.21 Ma, which is consistent with the hydrothermal muscovite $^{40}Ar/^{39}Ar$ plateau age of 13.68 ± 0.17 Ma. The granite porphyries are shoshonitic in composition. There are enriched in Ba, LREE, and Sr, and depleted in MgO and Cr, and display slightly negative Eu anomalies and positive LILEs and HFSEs anomalies. The zircon grains have $\varepsilon_{Hf}(t)$ values of −8.78 to −5.01 and TDM2 range from 1410 to 1648 Ma. The major and trace elements and Hf isotopic data of the granite porphyries indicate that the primitive magmas were produced by high extent partial melting of an ancient crust source. A comparison of the granite porphyries at Siruyidie'er prospect with Eocene to Miocene ore-forming granitic porphyries of the Tibetan plateau reveals that Siruyidie'er prospect has a potential to form porphyry Mo ± Cu but not porphyry Cu ± Mo ± Au deposit as the granite porphyries at Siruyidie'er prospect have low water contents and originated from an ancient continental crust rather than a depleted mantle source.

Acknowledgments

Financial support for this research was provided by the National Key Research and Development Program of China (Grant No. 2017YFC0601403) and by the International Postdoctoral Exchange Fellowship Program 2017. We are grateful to three anonymous reviewers for their insightful reviews and comments, which helped improve an earlier version of this manuscript.

Appendix A. Supplementary data

Supplementary data to this article can be found online at https://doi.org/10.1016/j.oregeorev.2019.01.009.

Reference

Ballard, J.R., Palin, M.J., Campbell, I.H., 2002. Relative oxidation states of magmas inferred from Ce(IV)/Ce(III) in zircon: application to porphyry copper deposits of northern Chile. Contrib. Miner. Petrol. 144, 347–364.

Blichert-Toft, J., Albarède, F., 1997. The Lu-Hf isotope geochemistry of chondrites and the evolution of the mantle-crust system. Earth Planet. Sci. Lett. 148, 243–258.

Blichert-Toft, J., Chauvel, C., Albarède, F., 1997. Separation of Hf and Lu for high-precision isotope analysis of rock samples by magnetic sector-multiple collector ICP-MS. Contrib. Miner. Petrol. 127, 248–260.

Burtman, V.S., Molnar, P.H., 1993. In: Geological and Geophysical Evidence for Deep Subduction of Continental Crust Beneath the Pamir, pp. 1–76.

Byrne, K., Tosdal, R.M., 2014. Genesis of the late triassic southwest zone breccia-hosted alkalic porphyry Cu-Au deposit, Galore Creek, British Columbia, Canada. Econ. Geol. 109, 915–938.

Candela, P.A., 1997. A review of shallow, ore-related granites: textures, volatiles, and ore metals. J. Petrol. 38, 1619–1633.

Cao, K., Bernet, M., Wang, G.C., van der Beek, P., Wang, A., Zhang, K.X., Enkelmann, E., 2013. Focused Pliocene-Quaternary exhumation of the Eastern Pamir domes, western China. Earth Planet. Sci. Lett. 363, 16–26.

Chapman, J.B., Scoggin, S.H., Kapp, P., Carrapa, B., Ducea, M.N., Worthington, J., Oimahmadov, I., Gadoev, M., 2018. Mesozoic to Cenozoic magmatic history of the Pamir. Earth Planet. Sci. Lett. 482, 181–192.

Chen, Y.J., Pirajno, F., Li, N., Guo, D.S., Lai, Y., 2009. Isotope systematics and fluid inclusion studies of the Qiyugou breccia pipe-hosted gold deposit, Qinling Orogen, Henan province, China: implications for ore genesis. Ore Geol. Rev. 35, 245–261.

DeCelles, P., Kapp, P., Quade, J., Gehrels, G., 2011. Oligocene-Miocene Kailas basin, southwestern Tibet: record of postcollisional upper-plate extension in the Indus-Yarlung suture zone. GSA Bull. 123, 1337–1362.

Defant, M.J., Drummond, M.S., 1990. Derivation of some modern arc magmas by melting of young subducted lithosphere. Nature 347, 662–665.

Ding, L., Kapp, P., Wan, X., 2005. Paleocene-Eocene record of ophiolite obduction and initial India-Asia collision, south central Tibet. Tectonics 24.

Ducea, M.N., Lutkov, V., Minaev, V.T., Hacker, B., Ratschbacher, L., Luffi, P., Schwab, M., Gehrels, G.E., McWilliams, M., Vervoort, J., 2003. Building the Pamirs: the view from the underside. Geology 31, 849–852.

Fowler, M., Kocks, H., Darbyshire, D., Greenwood, P., 2008. Petrogenesis of high Ba–Sr plutons from the northern highlands Terrane of the British Caledonian Province. Lithos 105, 129–148.

Frikken, P.H., Cooke, D.R., Walshe, J.L., Archibald, D., Skarmeta, J., Serrano, L., Vargas, R., 2005. Mineralogical and isotopic zonation in the Sur-Sur tourmaline breccia, Rio Blanco-Los Bronces Cu-Mo deposit, Chile: implications for ore genesis. Econ. Geol. 100, 935–961.

Griffin, W.L., Pearson, N.J., Belousova, E., Jackson, S.E., Van Achterbergh, E., O'Reilly, S.Y., Shee, S.R., 2000. The Hf isotope composition of cratonic mantle: LAM-MC-ICPMS analysis of zircon megacrysts in kimberlites. Geochim. Cosmochim. Acta 64, 133–147.

Griffin, W.L., Wang, X., Jackson, S.E., Pearson, N., O'Reilly, S.Y., Xu, X.S., Zhou, X.M., 2002. Zircon chemistry and magma mixing, SE China: in-situ analysis of Hf isotopes, Tonglu and Pingtan igneous complexes. Lithos 61, 237–269.

Hacker, B., Luffi, P., Lutkov, V., Minaev, V., Ratschbacher, L., Plank, T., Ducea, M., Patiño-Douce, A., McWILLIAMS, M., Metcalf, J., 2005. Near-ultrahigh pressure processing of continental crust: miocene crustal xenoliths from the Pamir. J. Petrol. 46, 1661–1687.

Hedenquist, J.W., Lowenstern, J.B., 1994. The role of magmas in the formation of hydrothermal ore deposits. Nature 370, 519.

Hermann, J., Spandler, C.J., 2007. Sediment melts at sub-arc depths: an experimental study. J. Petrol. 49, 717–740.

Hou, Z., Zaw, K., Pan, G.T., Mo, X.X., Xu, Q., Hu, Y.Z., Li, X.Z., 2007. Sanjiang Tethyan metallogenesis in SW China: tectonic setting, metallogenic epochs and deposit types. Ore Geol. Rev. 31, 48–87.

Hou, Z.Q., Duan, L.F., Lu, Y.J., Zheng, Y.C., Zhu, D.C., Yang, Z.M., Yang, Z.S., Wang, B.D., Pei, Y.R., Zhao, Z.D., 2015a. Lithospheric architecture of the Lhasa terrane and its control on ore deposits in the Himalayan-Tibetan orogen. Econ. Geol. 110, 1541–1575.

Hou, Z.Q., Yang, Z.M., Lu, Y.J., Kemp, A., Zheng, Y.C., Li, Q.Y., Tang, J.X., Yang, Z.S., Duan, L.F., 2015b. A genetic linkage between subduction-and collision-related porphyry Cu deposits in continental collision zones. Geology 43, 247–250.

Hou, Z.Q., Yang, Z.M., Qu, X.M., Meng, X.J., Li, Z.Q., Beaudoin, G., Rui, Z.Y., Gao, Y.F., Zaw, K., 2009. The Miocene Gangdese porphyry copper belt generated during post-collisional extension in the Tibetan Orogen. Ore Geol. Rev. 36, 25–51.

Hou, Z.Q., Zeng, P.S., Gao, Y.F., Du, A.D., Fu, D.M., 2006. Himalayan Cu–Mo–Au mineralization in the eastern Indo-Asian collision zone: constraints from Re–Os dating of molybdenite. Miner. Deposita 41, 33–45.

Hou, Z.Q., Zhang, H.R., 2015. Geodynamics and metallogeny of the eastern Tethyan metallogenic domain. Ore Geol. Rev. 70, 346–384.

Hu, Z.C., Liu, Y.S., Chen, L., Zhou, L., Li, M., Zong, K.Q., Zhu, L.Y., Gao, S., 2011. Contrasting matrix induced elemental fractionation in NIST SRM and rock glasses during laser ablation ICP-MS analysis at high spatial resolution. J. Anal. At. Spectrom. 26, 425–430.

Ji, W.H., Li, R.S., Chen, S.J., He, S.P., Zhao, Z.M., Bian, X.W., Zhu, H.P., Cui, J.G., Ren, J.G., 2011. The discovery of Palaeoproterozoic volcanic rocks in the Bulunkuoler Group from the Tianshuihai Massif in Xinjiang of Northwest China and its geological significance. Sci. China Earth Sci. 54, 61–72.

Jiang, Y.H., Jiang, S.Y., Ling, H.F., Dai, B.Z., 2006. Low-degree melting of a metasomatized lithospheric mantle for the origin of Cenozoic Yulong monzogranite-porphyry, east Tibet: geochemical and Sr–Nd–Pb–Hf isotopic constraints. Earth Planet. Sci. Lett. 241, 617–633.

Jiang, Y.H., Liu, Z., Jia, R.Y., Liao, S.Y., Zhou, Q., Zhao, P., 2012. Miocene potassic granite–syenite association in western Tibetan Plateau: implications for shoshonitic and high Ba–Sr granite genesis. Lithos 134, 146–162.

Kapp, P., DeCelles, P.G., Gehrels, G.E., Heizler, M., Ding, L., 2007. Geological records of the Lhasa-Qiangtang and Indo-Asian collisions in the Nima area of central Tibet. Geol. Soc. Am. Bull. 119, 917–933.

Kapp, P., Yin, A., Harrison, T.M., Ding, L., 2005. Cretaceous-Tertiary shortening, basin development, and volcanism in central Tibet. Geol. Soc. Am. Bull. 117, 865–878.

Kapp, P., Yin, A., Manning, C.E., Murphy, M., Harrison, T.M., Spurlin, M., Lin, D., Xi-Guang, D., Cun-Ming, W., 2000. Blueschist-bearing metamorphic core complexes in the Qiangtang block reveal deep crustal structure of northern Tibet. Geology 28, 19–22.

Ke, S., Mo, X.X., Luo, Z.H., Zhan, H.M., Liang, T., Li, L., Li, W.T., 2006. Petrogenesis and geochemistry of Cenozoic Taxkorgan alkalic complex and its geological significane. Acta Petrol. Sin. 221, 905–915.

Kooijman, E., Smit, M.A., Ratschbacher, L., Kylander-Clark, A.R., 2017. A view into crustal evolution at mantle depths. Earth Planet. Sci. Lett. 465, 59–69.

Kufner, S.-K., Schurr, B., Sippl, C., Yuan, X., Ratschbacher, L., Ischuk, A., Murodkulov, S., Schneider, F., Mechie, J., Tilmann, F., 2016. Deep India meets deep Asia: lithospheric indentation, delamination and break-off under Pamir and Hindu Kush (Central Asia). Earth Planet. Sci. Lett. 435, 171–184.

Landtwing, M.R., 2002. Evolution of the breccia-hosted porphyry Cu-Mo-Au deposit at agua rica, argentina: progressive unroofing of a magmatic hydrothermal system. Econ. Geol. Bull. Soc. Econ. Geol. 97, 1273–1292.

Lara, P., Oyhantçabal, P., Dadd, K., 2017. Post-collisional, Late Neoproterozoic, high-Ba-Sr granitic magmatism from the Dom Feliciano Belt and its cratonic foreland, Uruguay: petrography, geochemistry, geochronology, and tectonic implications. Lithos 277, 178–198.

Li, W., Chen, Y., Yuan, X., Schurr, B., Mechie, J., Oimahmadov, I., Fu, B., 2018. Continental lithospheric subduction and intermediate-depth seismicity: constraints from S-wave velocity structures in the Pamir and Hindu Kush. Earth Planet. Sci. Lett. 482, 478–489.

Li, X.H., Long, W.G., Li, Q.L., Liu, Y., Zheng, Y.F., Yang, Y.H., Chamberlain, K.R., Wan, D.F., Guo, C.H., Wang, X.C., 2010. Penglai zircon megacrysts: a potential new working reference material for microbeam determination of Hf-O isotopes and U-Pb age. Geostand. Geoanal. Res. 34, 117–134.

Liu, D., Zhao, Z.D., Zhu, D.C., Niu, Y.L., DePaolo, D.J., Harrison, T.M., Mo, X.X., Dong, G.C., Zhou, S., Sun, C.G., 2014. Postcollisional potassic and ultrapotassic rocks in southern Tibet: mantle and crustal origins in response to India-Asia collision and convergence. Geochim. Cosmochim. Acta 143, 207–231.

Liu, Y.S., Hu, Z.C., Zong, K.Q., Gao, C.G., Gao, S., Xu, J., Chen, H.H., 2010. Reappraisement and refinement of zircon U-Pb isotope and trace element analyses by LA-ICP-MS. Chin. Sci. Bull. 55, 1535–1546.

Ludwig, K.R., 2003. Isoplot/Ex, Version 3.0: A Geochronological Toolkit for Microsoft Excel. Geochronology Center Special Publication, Berkeley, California, Berkeley.

Mahéo, G., Blichert-Toft, J., Pin, C., Guillot, S., Pêcher, A., 2009. Partial melting of mantle and crustal sources beneath South Karakorum, Pakistan: implications for the Miocene geodynamic evolution of the India-Asia convergence zone. J. Petrol. 50, 427–449.

McCulloch, M.T., Rosman, K.J., De Laeter, J.R., 1977. The isotopic and elemental abundance of ytterbium in meteorites and terrestrial samples. Geochim. Cosmochim. Acta 41, 1703–1707.

Miller, C., Schuster, R., Klötzli, U., Frank, W., Purtscheller, F., 1999. Post-collisional potassic and ultrapotassic magmatism in SW Tibet: geochemical and Sr–Nd–Pb–O isotopic constraints for mantle source characteristics and petrogenesis. J. Petrol. 40, 1399–1424.

Mo, X.X., Hou, Z.Q., Niu, Y.L., Dong, G.C., Qu, X.M., Zhao, Z.D., Yang, Z.M., 2007. Mantle contributions to crustal thickening during continental collision: evidence from Cenozoic igneous rocks in southern Tibet. Lithos 96, 225–242.

Mo, X.X., Zhao, Z.D., Deng, J.F., Dong, G.C., Zhou, S., Guo, T.Y., Zhang, S.Q., Wang, L.L., 2003. Response of volcanism to the India-Asia collision. Earth Sci. Front. 10, 135–148.

Negredo, A.M., Replumaz, A., Villaseñor, A., Guillot, S., 2007. Modeling the evolution of continental subduction processes in the Pamir-Hindu Kush region. Earth Planet. Sci. Lett. 259, 212–225.

Ouyang, H.G., Song, L.S., Ye, H.S., Cao, J.Y., Cheng, Y.L., Dai, J.Y., Feng, C.L., Han, Z., Wang, X.P., Li, R.H., 2017. In: Ore-prospecting in the Southwestern Xinjiang. Institute of mineral resources, Chinese academy of geological sciences, Beijing, pp. 277 (in Chines with English abstract).

Peng, T.P., Wilde, S.A., Fan, W.M., Peng, B.X., 2013. Late Neoarchean potassic high Ba–Sr granites in the Taishan granite–greenstone terrane: petrogenesis and implications for continental crustal evolution. Chem. Geol. 344, 23–41.

Richards, J.P., 2009. Postsubduction porphyry Cu-Au and epithermal Au deposits: products of remelting of subduction-modified lithosphere. Geology 37, 247–250.

Richards, J.P., 2015. Tectonic, magmatic, and metallogenic evolution of the Tethyan orogen: from subduction to collision. Ore Geol. Rev. 70, 323–345.

Richards, J.P., Spell, T., Rameh, E., Razique, A., Fletcher, T., 2012. High Sr/Y magmas reflect arc maturity, high magmatic water content, and porphyry Cu ± Mo ± Au potential: examples from the Tethyan arcs of central and eastern Iran and western Pakistan. Econ. Geol. 107, 295–332.

Robinson, A.C., 2009. Geologic offsets across the northern Karakorum fault: implications for its role and terrane correlations in the western Himalayan-Tibetan orogen. Earth Planet. Sci. Lett. 279, 123–130.

Robinson, A.C., 2015. Mesozoic tectonics of the Gondwanan terranes of the Pamir plateau. J. Asian Earth Sci. 102, 170–179.

Robinson, A.C., Ducea, M., Lapen, T.J., 2012. Detrital zircon and isotopic constraints on the crustal architecture and tectonic evolution of the northeastern. Pamir. Tectonics 31.

Robinson, A.C., Yin, A., Manning, C.E., Harrison, T.M., Zhang, S.-H., Wang, X.-F., 2004. Tectonic evolution of the northeastern Pamir: constraints from the northern portion of the Cenozoic Kongur Shan extensional system, western China. Geol. Soc. Am. Bull. 116, 953–973.

Robinson, A.C., Yin, A., Manning, C.E., Harrison, T.M., Zhang, S.H., Wang, X.F., 2007.

Cenozoic evolution of the eastern Pamir: implications for strain-accommodation mechanisms at the western end of the Himalayan-Tibetan orogen. Geol. Soc. Am. Bull. 119, 882–896.
Ross, P.-S., Jébrak, M., Walker, B.M., 2002. Discharge of hydrothermal fluids from a magma chamber and concomitant formation of a stratified breccia zone at the Questa porphyry molybdenum deposit, New Mexico. Econ. Geol. 97, 1679–1699.
Söderlund, U., Patchett, P.J., Vervoort, J.D., Isachsen, C.E., 2004. The ^{176}Lu decay constant determined by Lu-Hf and U-Pb isotope systematics of Precambrian mafic intrusions. Earth Planet. Sci. Lett. 219, 311–324.
Schmidt, J., Hacker, B.R., Ratschbacher, L., Stübner, K., Stearns, M., Kylander-Clark, A., Cottle, J.M., Alexander, A., Webb, G., Gehrels, G., 2011. Cenozoic deep crust in the Pamir. Earth Planet. Sci. Lett. 312, 411–421.
Schwab, M., Ratschbacher, L., Siebel, W., McWilliams, M., Minaev, V., Lutkov, V., Chen, F., Stanek, K., Nelson, B., Frisch, W., 2004. Assembly of the Pamirs: age and origin of magmatic belts from the southern Tien Shan to the southern Pamirs and their relation to Tibet. Tectonics. https://doi.org/10.1029/2003TC001583.
Sillitoe, R.H., 1985. Ore-related breccias in volcanoplutonic arcs. Econ. Geol. 80, 1467–1514.
Sillitoe, R.H., 2010. Porphyry copper systems. Econ. Geol. 105, 3–41.
Sippl, C., Schurr, B., Yuan, X., Mechie, J., Schneider, F., Gadoev, M., Orunbaev, S., Oimahmadov, I., Haberland, C., Abdybachaev, U., 2013. Geometry of the Pamir-Hindu Kush intermediate-depth earthquake zone from local seismic data. J. Geophys. Res. Solid Earth 118, 1438–1457.
Sláma, J., Košler, J., Condon, D.J., Crowley, J.L., Gerdes, A., Hanchar, J.M., Horstwood, M.S., Morris, G.A., Nasdala, L., Norberg, N., 2008. Plešovice zircon-a new natural reference material for U-Pb and Hf isotopic microanalysis. Chem. Geol. 249, 1–35.
Smit, M.A., Ratschbacher, L., Kooijman, E., Stearns, M.A., 2014. Early evolution of the Pamir deep crust from Lu-Hf and U-Pb geochronology and garnet thermometry. Geology 42, 1047–1050.
Stearns, M., Hacker, B., Ratschbacher, L., Rutte, D., Kylander-Clark, A., 2015. Titanite petrochronology of the Pamir gneiss domes: implications for middle to deep crust exhumation and titanite closure to Pb and Zr diffusion. Tectonics 34, 784–802.
Steiger, R.H., Jäger, E., 1977. Subcommission on geochronology: convention on the use of decay constants in geo-and cosmochronology. Earth Planet. Sci. Lett. 36, 359–362.
Stern, R.J., 2002. Subduction zones. Reviews of geophysics.
Sun, W.D., Huang, R.F., Li, H., Hu, Y.B., Zhang, C.C., Sun, S.J., Zhang, L.P., Ding, X., Li, C.Y., Zartman, R.E., 2015. Porphyry deposits and oxidized magmas. Ore Geol. Rev. 65, 97–131.
Tarney, J., Jones, C., 1994. Trace element geochemistry of orogenic igneous rocks and crustal growth models. J. Geol. Soc. 151, 855–868.
Van Hinsbergen, D.J., Lippert, P.C., Dupont-Nivet, G., McQuarrie, N., Doubrovine, P.V., Spakman, W., Torsvik, T.H., 2012. Greater India Basin hypothesis and a two-stage Cenozoic collision between India and Asia. Proc. Natl. Acad. Sci. 109, 7659–7664.
Wang, R., Richards, J.P., Hou, Z., Yang, Z., 2014. Extent of underthrusting of the Indian plate beneath Tibet controlled the distribution of Miocene porphyry Cu–Mo ± Au deposits. Miner. Deposita 49, 165–173.
Wang, S.S., 1983. Age determinations of ^{40}Ar-^{40}K, ^{40}Ar-^{39}Ar and radiogenic ^{40}Ar released characteristics on K-Ar geostandards of China. Sci. Geol. Sin. 315–323.
Wiedenbeck, M., Alle, P., Corfu, F., Griffin, W.L., Meier, M., Oberli, F., Quadt, A.V., Roddick, J.C., Spiegel, W., 1995. Three natural zircon standards for U-Th-Pb, Lu-Hf, trace element and REE analyses. Geostandards Newslett. 19, 1–23.
Wilkinson, J.J., 2013. Triggers for the formation of porphyry ore deposits in magmatic arcs. Nat. Geosci. 6, 917.
Xiao, L., Clemens, J.D., 2007. Origin of potassic (C-type) adakite magmas: experimental and field constraints. Lithos 95, 399–414.
Yang, F.W., 2007. Report of the detailed survey on Jilie Cu deposit, Taxkorgan, Xingjiang. Xi 'an zhongzheng mining information consulting co. LTD, Xingjiang, China, p. 49 (in Chinese).
Yang, W.Q., Liu, L., Cao, Y.T., Wang, C., He, S.P., Li, R.S., Zhu, X.H., 2010. Geochronological evidence of Indosinian (high-pressure) metamorphic event and its tectonic significance in Taxkorgan area of the Western Kunlun Mountains, NW China. Sci. China Earth Sci. 53, 1445–1459.
Yang, Z.M., Hou, Z.Q., Chang, Z.S., Li, Q.Y., Liu, Y.F., Qu, H.C., Sun, M.Y., Xu, B., 2016. Cospatial Eocene and Miocene granitoids from the Jiru Cu deposit in Tibet: petrogenesis and implications for the formation of collisional and postcollisional porphyry Cu systems in continental collision zones. Lithos 245, 243–257.
Yang, Z.M., Hou, Z.Q., White, N.C., Chang, Z.S., Li, Z.Q., Song, Y.C., 2009. Geology of the post-collisional porphyry copper–molybdenum deposit at Qulong, Tibet. Ore Geol. Rev. 36, 133–159.
Yang, Z.M., Hou, Z.Q., Xu, J.F., Bian, X.F., Wang, G.R., Yang, Z.S., Tian, S.H., Liu, Y.C., Wang, Z.L., 2014. Geology and origin of the post-collisional Narigongma porphyry Cu–Mo deposit, southern Qinghai, Tibet. Gondwana Res. 26, 536–556.
Yin, A., Harrison, T.M., 2000. Geologic evolution of the Himalayan-Tibetan orogen. Annu. Rev. Earth Planet. Sci. 28, 211–280.
Yuan, H.L., Gao, S., Dai, M.N., Zong, C.L., Günther, D., Fontaine, G.H., Liu, X.M., Diwu, C.R., 2008. Simultaneous determinations of U-Pb age, Hf isotopes and trace element compositions of zircon by excimer laser-ablation quadrupole and multiple-collector ICP-MS. Chem. Geol. 247, 100–118.
Zhang, C.L., Zou, H.B., Ye, X.T., Chen, X.Y., 2018. Tectonic evolution of the NE section of the Pamir Plateau: new evidence from field observations and zircon U-Pb geochronology. Tectonophysics 723, 27–40.
Zhang, L.C., Feng, J., Dong, L.H., Zhu, M.T., Zheng, M.T., Li, Z.Q., Hao, Y.H., Shi, Y.J., 2016. Deposit types, origin and metallogenetic regularity of Taxkorgan iron ore belt in West Kunlun. J. Earth Sci. Environ. 38, 427–443 (in Chinese with English abstract).
Zhou, Z.J., Tang, H.S., Chen, Y.J., Chen, Z.L., 2017. Trace elements of magnetite and iron isotopes of the Zankan iron deposit, westernmost Kunlun, China: a case study of seafloor hydrothermal iron deposits. Ore Geol. Rev. 80, 1191–1205.